Microcontinuum approach to multiscale modeling of multiphase reactive flow during mineral dissolution

Zhiying Liu (刘志颖),[1] Qianghui Xu (许强辉) ⦾,[2,*] Junyu Yang (杨君宇) ⦾,[3,†]
Kai H. Luo (罗开红) ⦾,[1,3] and Lin Shi (史琳)[1]

[1]*Key Laboratory for Thermal Science and Power Engineering of the Ministry of Education,
Department of Energy and Power Engineering, Tsinghua University, Beijing 100084, China*
[2]*School of Mechanical Engineering, Beijing Institute of Technology, Beijing 100081, China*
[3]*Department of Mechanical Engineering, University College London, Torrington Place,
London WC1E 7JE, United Kingdom*

Image-based modeling of mineral dissolution poses challenges due to its multiscale nature, requiring the consideration of multiphase reactive flow and transport at both the resolved pore scale (macropores/fractures) and the unresolved Darcy scale (micropores). The existing hybrid-scale simulation methods pose difficulties in handling the multiscale fluid-rock interactions and temporal structural evolution. In this study, we propose a multiscale compressive continuum species transfer (MC-CST) scheme to address the limitations of the standard CST scheme, which exhibits numerical diffusion issues at the gas-liquid interface and thereby suffers from inaccuracies in reactive transport simulations. The proposed scheme incorporates an additional compressive term derived from volume-averaging principles for the advection and diffusion fluxes in a single-field framework. To ensure the impermeable species transport condition at the solid boundary, a concentration extrapolation algorithm is developed. Four validation cases are conducted to demonstrate the model's capability in accurately simulating multiphase reactive flow and transport at various scales, including pore scale, continuum scale, and hybrid scales. Special attention is given to accurately modeling the thermodynamic conditions at the gas-liquid interface, particularly with respect to the concentration jump under conditions of large local Péclet numbers. Furthermore, we present a case study simulating calcite dissolution in a porous medium to underscore the importance of multiscale fluid-rock interactions for an in-depth comprehension of the dissolution regime.

I. INTRODUCTION

Mineral dissolution is widely encountered in many subsurface applications, including CO_2 geological storage and petroleum reservoir engineering [1–4]. For example, the injected CO_2 dissolves into the formation water during CO_2 geological storage, leading to calcite (a type of carbonate mineral) dissolution, which plays a crucial role in trapping and immobilizing the CO_2 [5]. Acidic fluids, such as hydrochloric acid, are often injected into reservoirs to dissolve minerals obstructing pore spaces, thereby increasing permeability and enhancing oil or gas recovery [6]. Depending on the specific flow conditions, pore geometry, and mineral properties, various dissolution patterns can arise, including facial dissolution, viscous fingering, conical wormholes, and ramified wormholes

---

*Corresponding author: xuqh12@bit.edu.cn

†Corresponding author: junyu.yang@ucl.ac.uk

　　　　　　043801-1

[6,7]. These physical changes in pore structure hold a substantial influence on the subsurface processes, thereby necessitating an in-depth study. Notably, pore-resolved numerical modeling allows for direct consideration of the explicit pore geometry within complex porous media, thereby advancing our quantitative understanding of the nonlinear fluid-rock interaction during multiphase reactive flow and transport in mineral dissolution [8].

The multiscale feature of natural geological structures presents significant challenges for numerical modeling, even within pore-resolved computational domains of centimeter scale [9]. The size of natural pores and fractures can span several orders of magnitude, ranging from submicrometer to several hundred micrometers [10]. High-resolution imaging techniques, such as x-ray computed microtomography (micro-CT), enable nondestructive reconstruction of detailed pore spaces and mineral grains. This digital representation of the rock microstructure is commonly referred to as digital rock, and its accompanying pore-scale simulations offer great potential for understanding fluid-rock interactions during mineral dissolution [11,12]. However, achieving a full Navier-Stokes modeling for all pore spaces characterized via digital rock techniques would result in an unacceptable computational burden. More importantly, there are tradeoffs between image resolution and sample size. For example, when scanning a typical core plug of 2.5 cm in diameter, micrometer-scale pores can be explicitly resolved while a significant number of sub-micrometer-scale pores remain hidden below the image voxel [13,14]. In contrast to the resolved pore space, the unresolved porous medium is typically treated as an effective continuum with subgrid information, including porosity, saturation, and permeability [15–17]. Neglecting the reactive flow within the subresolution porous medium can lead to the oversight of important phenomena such as the development of a weathered zone near the fracture-porous interface [18]. Consequently, modeling complications arise from the combined pore-resolved and continuum-scale representations of such digital rocks.

Multiphase reactive flow involves the coupling of advection-dominated and diffusion-dominated mechanisms at multiple scales. In fully resolved macropores/fractures with high fluid transport capacity, inertial and viscous forces dominate the multiphase flow [15,19], resulting in high Péclet numbers (Pe, a dimensionless number quantifying the relative importance of advection to diffusion in a system) [6]. The high Péclet number condition signifies that convective transport becomes more significant than molecular diffusion. Conversely, within unresolved micropores characterized by reduced size and permeability, capillary forces gradually dominate the slower multiphase flow, leading to much lower Péclet numbers, typically below 10^{-1}. As such, the molecular diffusion and the possible Knudsen diffusion become the primary mechanisms [20], overshadowing the influence of advection transport. In the conventional single-scale simulation [21], the porous mineral matrix was typically considered as impermeable solid structures, neglecting the smaller-scale reactive transport processes. However, this approach may lead to a misinterpretation of dissolution dynamics under different conditions given the insufficient account of the scale-dependent processes and their mutual mass transfer within the complex spatial arrangements of the multiscale pore space [10,22,23]. The challenge of dynamic dissolution also involves the movement of fluid-solid interfaces and the microstructural evolution of the subresolution porous matrix. Therefore, predictive modeling of multiphase reactive flow through the inherently multiscale porous media remains highly challenging. To the best of our knowledge, few studies have been devoted to understanding the multiscale dynamics of multiphase reactive flow during mineral dissolution. This status primarily arises from the limited development of numerical modeling and methodologies applied in this field.

Hybrid-scale modeling provides a powerful approach for image-based simulations of multiscale flow and transport, which can be broadly classified into two categories: the domain decomposition method and the microcontinuum method [9]. In the domain decomposition method, the computational domain is decomposed into separate subdomains comprising resolved solid-free regions (e.g., macropores and fractures) and unresolved porous matrix. Two independent sets of governing equations and numerical models are applied to adapt the scale-dependent representations of the porous media and account for different flow and transport physics. In this approach, the standard Navier-Stokes/Stokes equation·and advection-diffusion equations are used to describe the single-phase/multiphase flow and solute transport in the solid-free regions [24]. On the other hand, the

flow and transport in the porous matrix are solved using continuum-scale models based on Darcy's law, supplemented by subgrid models such as the absolute/relative permeability model, the reactive surface area model, and the capillary pressure model [9,25]. Bidirectional communication between at-scale modeling domains is implemented during scale coupling to enforce physical continuity through appropriate interaction algorithms and boundary conditions, such as the Beavers and Joseph interface condition [18,26]. Molins *et al.* [25] developed the domain decomposition method and applied it to simulate the multiscale reactive transport in fractured media, where the dissolution occurs in both the fracture and the matrix. The multiscale model was proved to effectively simulate altered layers that formed around the porous matrix and the nonequilibrium concentration at the calcite surface under surface-limited reaction conditions, which cannot be captured by the purely pore-scale simulation. However, the domain decomposition method currently faces challenges in capturing the dynamic evolution of the interface between pore- and continuum-scale subdomains as a result of dissolution [25,27]. Further development of coupling theories, non-iterative solutions, and local grid refinement algorithms is required to enhance the model's performance in realistic multiphase problems with dynamic morphology [9].

Compared to the domain decomposition method, the microcontinuum model differs primarily in that it employs single-field governing equations capable of describing multiscale physics throughout the entire computational domain, regardless of the content within each grid cell. The fundamental aspect of the microcontinuum framework is the local porosity field ε_f to map the multiscale structure. A bounding value of $\varepsilon_f = 1$ represents the resolved pores/fractures, while a bounding value $\varepsilon_f = 0 \equiv 0.01$ characterizes the impermeable solid. The intermediate range $0 < \varepsilon_f < 1$ describes the unresolved pores [19]. Numerous numerical studies have leveraged the Darcy-Brinkmann-Stokes (DBS) momentum equation in the microcontinuum framework to demonstrate its capacity in modeling single-phase flows across multiscale porous media [6,13,20,24,28]. Additionally, the multiphase microcontinuum DBS framework has been developed to simulate multiphase flows across the multiscale porous media. Two-phase microcontinuum DBS frameworks can be tracked back to the work of Horgue *et al.* [29] and Soulaine *et al.* [16,17], who proposed multiphase DBS equations to describe the two-phase flow at both the pore and continuum scales. Carrilo *et al.* [15] later proposed an improved multiphase microcontinuum model, wherein theoretical derivations were rooted in elementary physics and volume-averaging principles. According to the rigorous derivations of multiscale parameters, including the relative velocity, density, and capillary force, the multiphase microcontinuum model was validated to asymptotically match the scale-dependent multiphase model. This includes the classic volume-of-fluid (VOF) -based Navier-Stokes model at the pore scale and the multiphase Darcy's model at the continuum scale. Recently, Liu *et al.* improved the two-phase microcontinuum DBS models to mitigate spurious velocities at the gas-liquid interface and contact-line regions, strengthening the modeling accuracy of the capillary-dominated multiphase flow [19]. Thanks to these efforts, the multiphase microcontinuum model becomes feasible for solving multiphase flow across the multiscale porous media.

Nevertheless, the modeling of multiphase reactive flow and transport in the microcontinuum framework is still in its infancy. Soulaine *et al.* employed the microcontinuum approach to simulate mineral dissolution in presence of gas and liquid phases [17]. However, the focus of these simulations was on the dynamic evolution of the fluid-solid interface without incorporating any complex remeshing strategies. Moreover, due to the absence of continuum-scale physics in the porous matrix ($0 < \varepsilon_f < 1$), the model was equivalent to a pore-scale model with an embedded boundary method for time-evolving domains. The challenge lies in the modeling of multispecies transport with interfacial mass transfer in realistic multiscale domains. To be more specific, the single-field concentration equation must be formulated to ensure the continuity of fluxes and chemical potentials at the gas-liquid interface in both the pore-scale and continuum-scale regions, regardless of the transport mechanisms dominated by advection or diffusion. Recent progress on pore-scale modelings of the multiphase mass transport can provide some insights into the multiscale modeling in the microcontinuum framework. At the pore scale, the volume-of-fluid (VOF) framework introduced the continuum species transfer (CST) approach proposed by Haroun [30] to enforce

interface conditions. However, Yang *et al.* found that the original CST method can significantly violate mass conservation when convection dominates diffusion locally near the interface (local Péclet number $Pe_{local} > 0.5$) [31]. Later, Maes *et al.* developed a compressive continuum species transfer scheme, known as C-CST, to achieve more robust simulations across a wide range of Péclet numbers [32]. Despite the advancements of CST methods at pore scale, less attention has been paid to the multiphase microcontinuum model, leading to its limited capability to perform the advection-dominated species transport with the interplay of the pore-scale and continuum-scale physics.

In this paper, the two-phase microcontinuum model is developed to robustly simulate the multiphase reactive flow and transport with interface species transfer. By employing volume averaging to the species transfer equation, rigorous derivations of single-field advection and diffusion fluxes are performed, yielding an additional compressive term compared to the previous microcontinuum CST model [17]. Several validation cases are then conducted to prove the model capacity for solving reactive flow and transport under varying Péclet number conditions at pore scale, continuum scale, and hybrid scales, respectively. Finally, a challenging application is simulated to study the calcite dissolution in a multiscale porous medium to improve the understanding of the multiscale fluid-rock interaction dynamics.

II. MATHEMATICAL MODELS

In this section, the mathematical model based on the microcontinuum DBS framework is developed to simulate the multiscale and multiphase dissolution, including mass, momentum, saturation, and concentration conservations. The concentration equation is derived using a multiscale compressive continuous species transfer scheme (MC-CST) to suppress the numerical diffusion by the convection term at both the pore and continuum scales.

A. Multiscale variable definitions

In the microcontinuum DBS framework, fluid and solid aggregates at a scale smaller than the control volume are filtered as the subgrid information. Thus, each control volume can contain one or two fluid phases (V_l/V_g) in resolved macropores, an impermeable solid phase (V_s), or unresolved fluid/solid aggregates ($V_l/V_g/V_s$). The volume fraction of void space in each control volume, namely the local porosity, is introduced as $\varepsilon_f = (V_l + V_g)/V$ to categorize the complex multiscale structure into the three regions: the resolved macropores ($\varepsilon_f = 1$), the unresolved porous matrix ($0 < \varepsilon_f < 1$), and the solid regions ($\varepsilon_f \approx 0$). Meanwhile, the saturation field is characterized as the ratio of the liquid volume over the total fluid phase volume within the control volume $\alpha_l = V_l/(V_l + V_g)$. In the resolved macropores, the saturation field is defined as the indicator function in the volume-of-fluid (VOF) model to track the gas-liquid interface delineated by $0 < \alpha_l < 1$, with the bounding values of $\alpha_l = 1$ and 0 as the liquid and gas phase, respectively. By contrast, the saturation field turns out to represent the actual liquid phase distribution as the multiphase Darcy equation in the unresolved porous matrix. Note that the relations $\varepsilon_f + \varepsilon_s = 1$ and $\alpha_l + \alpha_g = 1$ are always valid for all the computational cells. Therefore, only ε_s and α_l need to be computed to simulate the evolution of the mineral/pore structure and liquid/gas phase distribution.

According to volume averaging, governing partial differential equations are formulated in terms of single fields regardless of the cell content. Correspondingly, all the physical variables should be defined as the volume-averaged quantities over the control volume by $\bar{\beta}_i = (1/V) \int_{V_i} \beta_i dV$, or the phase-averaged quantities over each phase by $\bar{\beta}_i^i = (1/V_i) \int_{V_i} \beta_i dV$ ($i = l, g$). For example, $\bar{\boldsymbol{v}}_l$ depicts the averaged liquid velocity through the control volume, $\bar{p}_g^g$ denotes the averaged pressure over the gas phase, and $\bar{c}_{l,j}^l$ defines the averaged molar concentration of species j in the liquid phase.

These averages can be related to the local porosity and the saturation via $\bar{\beta}_i = \varepsilon_i \alpha_i \bar{\beta}_i^i$. In this context, the single-field pressure, velocity, and molar concentration can be derived as

$$\bar{p} = \alpha_l \bar{p}_l^l + \alpha_g \bar{p}_g^g, \tag{1}$$

$$\bar{\boldsymbol{v}} = \bar{\boldsymbol{v}}_l + \bar{\boldsymbol{v}}_g = \varepsilon_f \left(\alpha_l \bar{\boldsymbol{v}}_l^l + \alpha_g \bar{\boldsymbol{v}}_g^g \right), \tag{2}$$

$$\bar{c}_j = \alpha_l \bar{c}_{j,l}^l + \alpha_g \bar{c}_{j,g}^g. \tag{3}$$

B. Microcontinuum equations for two-phase flow

The microcontinuum equations for two-phase flow are implemented based on Carrillo's derivation [15], with numerical improvement in the previous work to reduce the spurious velocity [19]. In this section, the derivation from the fundamental equations to the upscaled equations and the numerical corrections are briefly reviewed.

Assuming the fluid phases are Newtonian, incompressible, and immiscible, the fundamental equations, including the mass and momentum conservation in each phase, dictate

$$\frac{\partial \rho_i}{\partial t} + \nabla \cdot (\rho_i \boldsymbol{v}_i) = 0, \quad i = l, g, \tag{4}$$

$$\frac{\partial \rho_i \boldsymbol{v}_i}{\partial t} + \nabla \cdot (\rho_i \boldsymbol{v}_i \boldsymbol{v}_i) - \nabla \cdot \boldsymbol{\tau}_i = -\nabla p_i + \rho_i g, \quad i = l, g, \tag{5}$$

where $\boldsymbol{v}_i$ is the velocity of phase i, $\boldsymbol{\tau}_i = (\mu_i (\nabla \boldsymbol{v}_i + \nabla \boldsymbol{v}_i^T))$ is the viscous stress tensor, μ_i is the viscosity of phase i, p_i is the pressure of phase i, and $\boldsymbol{g}$ is the gravity vector. At the gas-liquid interface with a velocity of $\boldsymbol{w}$, the mass conservation is expressed as

$$\rho_l(\boldsymbol{v}_l - \boldsymbol{w}) \cdot \boldsymbol{n}_{lg} = \rho_g(\boldsymbol{v}_g - \boldsymbol{w}) \cdot \boldsymbol{n}_{lg} \quad \text{at} \quad A_{lg}, \tag{6}$$

where ρ_i is the density of phase i, and $\boldsymbol{n}_{lg}$ is the normal vector to the fluid-fluid interface pointing from the wetting to the nonwetting phase. When there is no phase change at the fluid-fluid interface, $\boldsymbol{v}_l = \boldsymbol{v}_g = \boldsymbol{w}$. The surface tension causes a sharp interface pressure drop at the fluid-fluid interface,

$$\Delta p_c = p_g - p_l = \sigma \kappa \quad \text{at} \quad A_{lg}, \tag{7}$$

where p_g and p_l are the pressure of the nonwetting and wetting phase, σ is the surface tension coefficient, and $\kappa = \nabla \cdot \boldsymbol{n}_{lg}$ is the interface curvature.

The above fundamental equations are defined on a continuous physical domain. After discretizing the continuous domain into the grid-based domain by the finite volume method (FVM), the single-field microcontinuum model is derived using volume-averaging theorems,

$$\overline{\frac{\partial \beta_i}{\partial t}} = \frac{\partial \bar{\beta}_i}{\partial t} - \frac{1}{V} \int_{A_{i,f}} \beta_i \boldsymbol{v}_{i,f} \cdot \boldsymbol{n}_{i,f} dA - \frac{1}{V} \int_{A_{i,s}} \beta_i v_{i,s} \cdot \boldsymbol{n}_{i,s} dA, \tag{8}$$

$$\overline{\nabla \beta_i} = \nabla \bar{\beta}_i + \frac{1}{V} \int_{A_{i,f}} \beta_i \boldsymbol{n}_{i,f} dA + \frac{1}{V} \int_{A_{i,s}} \beta_i \boldsymbol{n}_{i,s} dA, \tag{9}$$

$$\overline{\nabla \cdot \beta_i} = \nabla \cdot \bar{\beta}_i + \int_{A_{i,f}} \beta_i \cdot \boldsymbol{n}_{i,f} dA + \frac{1}{V} \int_{A_{i,s}} \beta_i \cdot \boldsymbol{n}_{i,s} dA, \tag{10}$$

where subscripts f and s represent the fluid-fluid interface and the fluid-solid interface of phase i, respectively.

The application of the volume-averaging theorems on the mass conservation equation of each phase, Eq. (4), yields [33]

$$\frac{\partial \varepsilon_f \alpha_i}{\partial t} + \nabla \cdot (\alpha_i \bar{\boldsymbol{v}}_i) = 0, \quad i = l, g. \tag{11}$$

The single-field continuity equation is obtained by adding the volume-averaged mass conservation equation of each phase [33],

$$\boldsymbol{\nabla} \cdot \bar{\boldsymbol{v}} = 0. \tag{12}$$

A similar upscaling procedure is also performed to form the multiscale single-field momentum equation [33],

$$\frac{1}{\varepsilon_f}\left(\frac{\partial \rho \bar{\boldsymbol{v}}}{\partial t} + \boldsymbol{\nabla} \cdot \left(\frac{\rho}{\varepsilon_f}\bar{\boldsymbol{v}}\bar{\boldsymbol{v}}\right)\right) = -\boldsymbol{\nabla}\bar{p} + \rho g + \boldsymbol{\nabla} \cdot (\mu(\boldsymbol{\nabla}\bar{\boldsymbol{v}} + \boldsymbol{\nabla}\bar{\boldsymbol{v}}^T)) - \mu k^{-1}\bar{\boldsymbol{v}} + F_c, \tag{13}$$

where μk^{-1} is a drag force coefficient in unresolved porous regions, and $\mathbf{F}_c$ is the surface tension force in the fluid-fluid interface.

As to the specific modeling of the two-phase interfacial dynamics, the VOF method is employed to explicitly track the shape and position of the interface in the resolved macropore region. The averaged phase velocities $\bar{\boldsymbol{v}}_i$ in the volume-averaged mass conservation equations, Eq. (11), are transformed into expressions of the single-field variables, deriving the saturation equation [33],

$$\frac{\partial \varepsilon_f \alpha_l}{\partial t} + \boldsymbol{\nabla} \cdot (\alpha_l \bar{\boldsymbol{v}}) + \boldsymbol{\nabla} \cdot (\varepsilon_f \alpha_l \alpha_g \boldsymbol{v}_r) = 0, \tag{14}$$

where $\boldsymbol{v_r} = \bar{\boldsymbol{v}}_{\mathrm{l}}^{\mathrm{l}} - \bar{\boldsymbol{v}}_{\mathrm{g}}^{\mathrm{g}}$ is the relative velocity. Since there is no conservation law to solve for $\boldsymbol{v}_{\mathrm{r}}$, this term must be closed.

In resolved macropore regions, the relative velocity is computed using the gradient of the saturation and a value based on the maximum magnitude of $\bar{\boldsymbol{v}}$, which is a common practice in the VOF method,

$$\boldsymbol{v}_r = C_\alpha \max{(\bar{\boldsymbol{v}})}\left(\frac{\boldsymbol{\nabla}\alpha_l}{|\boldsymbol{\nabla}\alpha_l|}\right), \tag{15}$$

where C_α is the interface compression coefficient to adjust the magnitude of the compressive velocity normal to the gas-liquid interface for a tradeoff between the interface thickness and spurious velocity in the macropore regions. The continuum surface force (CSF) model is used for specific modeling of the interfacial force term arising from the VOF method [15],

$$\boldsymbol{F}_c = \varepsilon_f^{-1}\sigma \boldsymbol{\nabla} \cdot \left(\frac{\boldsymbol{\nabla}\alpha_l}{|\boldsymbol{\nabla}\alpha_l|}\right)\boldsymbol{\nabla}\alpha_l. \tag{16}$$

The multiphase Darcy equation is applied to describe the multiphase flow in unresolved micropore regions. The two-phase Darcy model and a capillary pressure model are used to derive the drag force coefficient, the relative velocity, and the surface tension force in unresolved micropore regions [15]. The momentum balance equations of the two-phase Darcy model can be written as

$$0 = -\boldsymbol{\nabla}\bar{p}_i^i + \rho_i g - M_i^{-1}\bar{\boldsymbol{v}}_i, \quad i = 1, \mathrm{g}, \tag{17}$$

where $M_i = \frac{k_0 k_{\mathrm{r},i}}{\mu_i}$ are the fluid mobilities, k_0 is the the absolute permeability of the porous structure, and $k_{\mathrm{r},i}$ are the relative permeabilities of each phase.

The microcontinuum framework is used to combine the above equations and models of both the macropore and micropore regions into a fully coupled multiscale model, which can be applied in pore, continuum, or hybrid scale representation of multiphase flow in porous media. The multiscale parameters, $\boldsymbol{v}_{\mathrm{r}}$, ρ, μk^{-1}, and $\boldsymbol{F}_{\mathrm{c}}$, are defined to illustrate Eqs. (13) and (14) by asymptotic matching to the VOF method in resolved macropore regions and to the multiphase Darcy model in unresolved micropore regions.

According to Carrillo's work, the multiscale relative velocity $\boldsymbol{v}_r$ is expresseas [15]

$$\boldsymbol{v}_r = \begin{cases} C_\alpha \max(|\bar{\boldsymbol{v}}|)\frac{\nabla\alpha_l}{\nabla\alpha_l} & \text{in resolved macropore regions,} \\ \varepsilon_f^{-1}\begin{bmatrix} -\left(\frac{M_l}{\alpha_l} - \frac{M_g}{\alpha_g}\right)\nabla\bar{p} + \left(\frac{\rho_l M_l}{\alpha_l} - \frac{\rho_g M_g}{\alpha_g}\right)\boldsymbol{g} \\ +\left(\frac{M_l\alpha_g}{\alpha_l} + \frac{M_g\alpha_l}{\alpha_g}\right)\nabla p_c - \left(\frac{M_l}{\alpha_l} - \frac{M_g}{\alpha_g}\right)p_c\nabla\alpha_l \end{bmatrix} & \text{in unresolved porous regions,} \end{cases} \tag{18}$$

where p_c is the capillary pressure. According to the two-phase Darcy law, the relative velocity $\boldsymbol{v}_r$ in the porous domain can be formulated to account for the comprehensive interplay of the relative permeability, gravity, and capillary effects.

The multiscale density ρ and drag force coefficient μk^{-1} can be written as [15]

$$\rho = \begin{cases} \rho_l\alpha_l + \rho_g\alpha_g & \text{in resolved macropore regions,} \\ (\rho_l M_l + \rho_g M_g)M^{-1} & \text{in unresolved porous regions,} \end{cases} \tag{19}$$

$$\mu k^{-1} = \begin{cases} 0 & \text{in resolved macropore regions,} \\ k_0^{-1}\left(\frac{k_{\mathrm{r,l}}}{\mu_l} + \frac{k_{\mathrm{r,g}}}{\mu_g}\right)^{-1} & \text{in unresolved porous regions,} \end{cases} \tag{20}$$

where $M = M_l + M_g$ is the total mobility. Notably, the single-fluid density is the saturation-weighted average in resolved macropore regions, while it becomes the mobility-weighted average in unresolved micropore regions. The absolute permeability is usually described by the Kozeny-Carman relation with respect to the local porosity, while the relative permeability for different saturations can be given by the Brooks and Corey model [34]. Correspondingly, the nonzero drag force coefficient μk^{-1}, based on a harmonic average of the two-phase mobilities, is applied exclusively in the porous regions to describe the porous resistance exerted on the subgrid pore walls.

The multiscale capillary force $\mathbf{F}_c$ follows the relation as [15]

$$\boldsymbol{F}_c = \begin{cases} -\varepsilon_f^{-1}\sigma\nabla\cdot(n_{\mathrm{lg}})\nabla\alpha_l & \text{in resolved macropore regions,} \\ \left[M^{-1}(M_l\alpha_g - M_g\alpha_l)\left(\frac{\partial p_c}{\partial\alpha_l}\right) - p_c\right]\nabla\alpha_l & \text{in unresolved porous regions,} \end{cases} \tag{21}$$

where σ is the surface tension, $n_{\mathrm{lg}} = \frac{\nabla\alpha_l}{\nabla\alpha_l}$ is the normal to the gas-liquid interface, and p_c is the capillary pressure. In the macropores, the capillary force $\boldsymbol{F}_c$ reduces to the well-known continuum surface force (CSF) formulation to balance the pressure gradient according to Young-Laplace law. In the unresolved porous domain, the capillary force $\boldsymbol{F}_c$ is derived such that the DBS momentum equation can match the two-phase Darcy equation [15]. The relationship between the capillary pressure and the saturation can be given by the Van Genutchen model [35].

In the multiphase microcontinuum DBS framework, liquid-statured or gas-saturated porous regions impact the saturation gradient at the porous boundary, which results in an unintended normal to the gas-fluid interface. Some numerical corrections were proposed to improve the numerical accuracy of the interface curvature and reduce the spurious velocity around the gas-liquid interface [19].

The face-centered interface norm $\boldsymbol{n}_{\mathrm{lg},f}$ is employed to calculate the term $\nabla\cdot(\boldsymbol{n}_{lg})$ (the magnitude of the interface curvature) based on the Gaussian scheme. A hybrid numerical scheme is used to compute $n_{lg,f}$ more accurately as follows [19]:

$$n_{\mathrm{lg},f} = C\left\langle\frac{\nabla\alpha}{\|\nabla\alpha\|}\right\rangle_{c\to f} + (1 - C_{lg})\frac{\langle\nabla\alpha_l\rangle_{c\to f}}{\|\langle\nabla\alpha_l\rangle_{c\to f}\|_{lg}}, \tag{22}$$

where C_{lg} is the mixing coefficient, set as 0.6 in this work, and $\langle\rangle_{c\to f}$ denotes the interpolation operator from the cell-centered field to the face-centered field.

At the porous/solid boundary, a saturation extrapolation algorithm is devised to reconstruct the saturation gradient in the gas-liquid interface before modifying $\boldsymbol{n}_{lg}$ to enforce the wall adhesion

condition with the prescribed contact angle θ by

$$\tilde{\boldsymbol{n}}_{\text{lg}} = \frac{\cos \theta - \cos \theta_{\text{I}} \cos (\theta_{\text{I}} - \theta)}{1 - \cos^2 \theta_{\text{I}}} \boldsymbol{n}_{\text{p}} + \frac{\cos (\theta_{\text{I}} - \theta) - \cos \theta_{\text{I}} \cos \theta}{1 - \cos^2 \theta_{\text{I}}} \boldsymbol{n}_{\text{lg}}, \tag{23}$$

where $\tilde{\boldsymbol{n}}_{lg}$ is the local modified normal vector, $\boldsymbol{n}_p = \frac{\nabla \varepsilon_f}{\|\nabla \varepsilon_f\|}$ is the normal to the porous boundary, and $\theta_{\text{I}} = \cos^{-1}(\boldsymbol{n}_p \cdot \boldsymbol{n}_{\text{lg}})$ is the contact angle before correction. To reduce the spurious velocity at the contact line, $\boldsymbol{n}_{\text{lg}}$ should be first revised based on the extrapolated saturation from resolved macropore regions to the nearby porous region [19],

$$\chi = \begin{cases} 1 & \text{in resolved macropore regions,} \\ 0 & \text{in unresolved pore regions,} \end{cases} \quad \chi_f = \lceil \langle \chi \rangle_{c \rightarrow f} \rceil, \tag{24}$$

$$\alpha_{\text{l,corr}} = \begin{cases} \chi \alpha_{\text{l}} + (1 - \chi) \frac{\langle \chi_f \langle \alpha_{\text{l}} \rangle_{c \rightarrow f, \text{harmonic}} \rangle_{f \rightarrow c}}{\langle \chi_f \rangle_{f \rightarrow c}}, & \alpha_{\text{l,solid}} = 1 \\ 1 - \left(\chi(1 - \alpha_{\text{l}}) + (1 - \chi) \frac{\langle \chi_f (1 - \alpha_{\text{l}})_{c \rightarrow f, \text{harmonic}} \rangle_{f \rightarrow c}}{\langle \chi_f \rangle_{f \rightarrow c}} \right), & \alpha_{\text{l,solid}} = 0 \end{cases}, \tag{25}$$

where χ is an indicator function representing whether the grid block belongs to the resolved macropore region or the unresolved porous region, $\lceil \rceil$ denotes the ceiling operator that maps a real number x to the smallest integer greater than or equal to x, $\langle \rangle_{f \rightarrow c}$ represents interpolation from face center to cell center, while $\langle \rangle_{c \rightarrow f}$ represents interpolation from cell center to face center. The subscript "harmonic" denotes the harmonic-mean scheme used in the interpolation. Meanwhile, $\boldsymbol{n}_{\text{p}}$ is numerically smoothed to improve its perpendicularity to the curved and sloped porous boundary by [19]

$$\tilde{\boldsymbol{n}}_p^* = \frac{\|\boldsymbol{n}_p\| \langle \langle \xi \boldsymbol{n}_p \rangle_{c \rightarrow f} \rangle_{f \rightarrow c}}{\langle \langle \xi \rangle_{c \rightarrow f} \rangle_{f \rightarrow c}}. \tag{26}$$

C. Mineral dissolution model

Following the experimental and numerical work by Soulaine *et al.* [17], mineral dissolution is simplified as reaction kinetics Eq. (27), in which the calcite crystal is acidified by the hydrochloric acid (HCl). The underlying assumption is that the CO_2 can be instantaneously nucleated at the mineral surface from the liquid phase to the gas phase,

$$CaCO_{3(s)} + 2HCl_{(l)} \rightarrow CaCl_{2(l)} + CO_{2(g)} + H_2O_{(l)}. \tag{27}$$
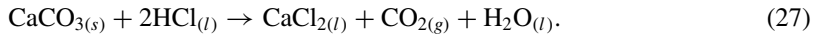
HCl is the primary species in the liquid phase, and the molar reaction rate $\dot{\boldsymbol{n}}_{\text{HCl}}$ can be written as

$$\dot{\boldsymbol{n}}_{\text{HCl}} = -r a_v^l (\bar{c}_{\text{HCl}} - \bar{c}_{\text{HCl,eq}}), \tag{28}$$

where r is the reaction rate constant, $\bar{c}_{\text{HCl}}$ is the averaged HCl molar concentration, and $\bar{c}_{\text{HCl,eq}}$ is the equilibrium concentration, respectively. Considering that the HCl is only present in the aqueous phase, the specific reactive surface a_v^l denotes the effective calcite area exposed to the acidic solution and it can be related by the specific geometrical area a_v and the liquid saturation α_l by $a_v^l = a_v \alpha_l$. In the present study, the specific geometrical area is modeled by the sugar lump model as Eq. (29) to account for the temporal evolution of the reactive surface area,

$$a_v = \left(a_{v0} + a_{vm} \left(1 - \left(\frac{\varepsilon_s}{\varepsilon_{s0}} \right)^{n_1} \right)^{n_2} \right) \left(\frac{\varepsilon_s}{\varepsilon_{s0}} \right)^{n_3}, \tag{29}$$

where a_{v0} is the initial specific surface area, a_{vm} is the maximum specific surface area by the sum of individual grain surface areas, ε_{s0} is the initial volume fraction of the calcite, and n_1, n_2, and n_3 are empirical coefficients of the specific microstructure of the calcite aggregates.

The volume fractions of the gas/liquid/solid phase are evolved during the mineral dissolution, and their evolution can be governed by the following conservations

laws:

$$\frac{\partial \varepsilon_s \rho_s}{\partial t} = \dot{m}_s, \tag{30}$$

$$\frac{\partial \varepsilon_f \alpha_i \rho_i}{\partial t} + \nabla \cdot \left(\varepsilon_f \alpha_i \rho_l \bar{\boldsymbol{v}}_i^i \right) = \dot{m}_i, \quad i = 1, \text{g}, \tag{31}$$

where ρ_s and ρ_i are the density of the solid and fluid phases, and $\dot{m}_s$ and $\dot{m}_i$ are the dissolution rate for the solid and fluid phases, respectively. These dissolution rates can be expressed based on the consumption rate of HCl $\dot{m}_{\text{HCl}}$ as

$$\dot{m}_{\text{HCl}} = M_{\text{HCl}} \dot{\boldsymbol{n}}_{\text{HCl}}, \tag{32}$$

$$\dot{m}_k = \gamma_k \dot{m}_{\text{HCl}}, \quad k = s, \, l, \, \text{g}. \tag{33}$$

γ_k is the stoichiometric coefficients: $\gamma_s = \frac{M_{\text{CaCO}_3}}{2M_{\text{HCl}}}$, $\gamma_g = \frac{-M_{\text{CO}_2}}{2M_{\text{HCl}}}$, and $\gamma_l = \frac{(2M_{\text{HCl}} - M_{\text{CaCl}_2} - M_{H_2O})}{2M_{\text{HCl}}}$, and M_j is the molar mass of species j.

After considering the dissolution rate $\dot{m}_1$, the saturation equation, Eq. (14), becomes

$$\frac{\partial \varepsilon_f \alpha_l}{\partial t} + \nabla \cdot (\alpha_l \bar{\boldsymbol{v}}) + \nabla \cdot (\varepsilon_f \alpha_l \alpha_g \boldsymbol{v}_r) = \frac{\dot{m}_l}{\rho_l}. \tag{34}$$

Assuming the gas and liquid phases are incompressible, the summation of Eqs. (30) and (31) can yield the global mass conservation as

$$\nabla \cdot \bar{\boldsymbol{v}} = \dot{m}_{\text{HCl}} \left(\frac{\gamma_s}{\rho_s} + \frac{\gamma_g}{\rho_g} + \frac{\gamma_l}{\rho_l} \right). \tag{35}$$

D. Concentration conservation equations

In a two-phase system, the chemical species can be present in both gas and liquid phases. Assuming the solution is dilute, the fundamental equation for species transfer of species j in phase i reads

$$\frac{\partial c_{j,i}}{\partial t} + \nabla \cdot (c_{j,i} \boldsymbol{v}_i) - \nabla \cdot (D_{j,i} \nabla c_{j,i}) = \dot{\boldsymbol{n}}_j \quad \text{in} \Omega_i \quad (i = l, \, \text{g}), \tag{36}$$

where $D_{j,i}$ is the molecular diffusivity of species j in phase i, $\boldsymbol{F}_{j,i} = c_{j,i} \boldsymbol{v}_i$ is the advective term, $\boldsymbol{J}_{j,i} = -D_{j,i} \nabla c_{j,i}$ is the diffusive term, and $\dot{\boldsymbol{n}}_j$ is the source term due to the chemical reaction. In this work, the effect of the interfacial mass transfer on the multiphase flow is neglected based on the specific problem that the characteristic time of CO_2 mass transfer from the gas to the liquid phase is much longer than that of the CO_2 production from the calcite dissolution [17]. Following Maes *et al.*'s work [36], the source term due to interfacial mass transfer is also easily formulated and involved in Eqs. (35)

At the gas-liquid interface, the flux continuity and thermodynamic equilibrium condition can be modelled using Henry's law,

$$(c_{j,i}(\boldsymbol{v}_i - w) - D_{j,i} \nabla c_{j,i}) \cdot \boldsymbol{n}_{1\text{g}} = 0, \quad \text{at} \quad A_{1\text{g}}, \tag{37}$$

$$\bar{c}_{j,1}^l = H_j \bar{c}_{j,\text{g}}^g, \tag{38}$$

where w is the interface velocity, and H_j is Henry's constant of species j. Similar to the derivation of the single-field momentum equation, the global concentration conservation equation to solve $\bar{c}_j$ throughout the multiscale domain can be formulated based on volume averaging.

The application of the volume-averaging theorem, Eqs. (8)–(10), to the fundamental equations for species j, Eq. (36), yields

$$\frac{\partial \bar{c}_{j,i}}{\partial t} + \nabla \cdot (\bar{\boldsymbol{F}}_{j,i} + \bar{\boldsymbol{J}}_{j,i}) + \boldsymbol{D}_{if} + \boldsymbol{D}_{is} = 0, \tag{39}$$

where the last two terms on the left-hand side,

$$\boldsymbol{D}_{if} = \frac{1}{V} \int_{A_{if}} (\boldsymbol{F}_{j,i} + \boldsymbol{J}_{j,i}) \cdot \boldsymbol{n}_{if} dA = 0,$$

$$\boldsymbol{D}_{is} = \frac{1}{V} \int_{A_{is}} (\boldsymbol{F}_{j,i} + \boldsymbol{J}_{j,i}) \cdot \boldsymbol{n}_{is} dA = \frac{1}{V} \int_{A_{is}} \boldsymbol{J}_{j,i} \cdot \boldsymbol{n}_{is} dA, \tag{40}$$

where $\boldsymbol{D}_{if}$ is the species flux at the gas-liquid interface, equal to 0 imposed by the flux continuity, Eq. (37), $\boldsymbol{D}_{is}$ reflects the diffusion resistance exerted by the solid surface with nonslip boundary condition ($\boldsymbol{v}_i = 0$). The averaged intrinsic molecular diffusion term $\nabla \cdot \bar{\boldsymbol{J}}_{j,i}$ and the diffusion resistance term $\boldsymbol{D}_{is}$ are lumped into an effective molecular diffusion term [17]

$$\nabla \cdot \bar{\boldsymbol{J}}_{j,i} + \boldsymbol{D}_{is} = -\nabla \cdot (D_{j,i}^* \nabla \bar{c}_{j,i}), \tag{41}$$

where $D_{j,i}^*$ is the effective diffusion coefficient in porous media, accounting for microstructural effects, such as porosity and tortuosity [37]. For simplification, $D_{j,i}^* = \varepsilon_{\mathrm{f}} D_{j,i}$ are used in this work [17]. Eventually, if the spatial derivatives of the local porosity and saturation are neglected, the volume-averaged concentration equation for species j in phase i becomes

$$\frac{\partial \varepsilon_f \alpha_i \bar{c}_{j,i}^i}{\partial t} + \nabla \cdot \left(\varepsilon_f \alpha_i \bar{c}_{j,i}^i \bar{\boldsymbol{v}}_i^i \right) = \nabla \cdot \left(\varepsilon_f \alpha_i D_{j,i}^* \nabla \bar{c}_{j,i}^i \right). \tag{42}$$

This equation is valid everywhere regardless of the cell content. The sum of the volume-averaged concentration equations for the gas and liquid phases yields

$$\frac{\partial \varepsilon_f \bar{c}_j}{\partial t} + \nabla \cdot \left(\varepsilon_f \alpha_l \bar{c}_{j,1}^l \bar{\boldsymbol{v}}_l^l + \varepsilon_f \alpha_g \bar{c}_{j,\mathrm{g}}^g \bar{\boldsymbol{v}}_g^g \right) = \nabla \cdot \left(\varepsilon_f \alpha_l D_{j,1}^* \nabla \bar{c}_{j,1}^l + \varepsilon_f \alpha_g D_{j,\mathrm{g}}^* \nabla \bar{c}_{j,\mathrm{g}}^g \right). \tag{43}$$

Here, the upscaled concentration equation is obtained. For the equation to be solved, the following derivation further transforms the upscaled equation into the single-field equation based on definitions of the single-field $\bar{\boldsymbol{v}}$ and $\bar{c}_j$.

The combination of the advection term result in Eq. (44) with the detailed derivation in Appendix A 1,

$$\nabla \cdot \left(\varepsilon_f \alpha_l \bar{c}_{j,1}^l \bar{\boldsymbol{v}}_l^l + \varepsilon_f \alpha_g \bar{c}_{j,\mathrm{g}}^g \bar{\boldsymbol{v}}_g^g \right) = \nabla \cdot (\bar{c} \bar{\boldsymbol{v}}) + \nabla \cdot \left(\varepsilon_f \alpha_g \alpha_l \left(\bar{c}_{j,1}^l - \bar{c}_{j,\mathrm{g}}^g \right) \boldsymbol{v}_r \right), \tag{44}$$

where the first term on the right-hand side is the standard advection term in Soulaine *et al.* [17], and the second term is an additional term, namely the multiscale compressive advection term. Combining the single-field concentration definition $\bar{c}_j$, Eq. (3), and Henry's law, Eq. (38), the unknown phase-averaged concentration difference $\bar{c}_{j,1}^l - \bar{c}_{j,\mathrm{g}}^g$ can be derived based on the thermodynamic equilibrium assumption at the gas-liquid interface,

$$\bar{c}_{j,1}^l - \bar{c}_{j,\mathrm{g}}^g = \frac{(1 - H_j)\bar{c}_j}{\alpha_l H_j + \alpha_g}. \tag{45}$$

Equation (44) is derived without any assumption and is an exact formulation of the single-field species advection term. The compressive advection term is not zero at the gas-liquid interface with an artificial compressive velocity $\boldsymbol{v}_{\mathrm{r}} \neq 0$. Section IV will show if the compressive term is not involved, numerical errors can significantly break species concentration conservation, particularly when the local Pélect number ($\mathrm{Pe}_{\mathrm{local}} = v_{\mathrm{x}} \Delta / D_{j,i}$, where v_x is the velocity along the x direction, and Δ is the grid size along the x direction) is large or even infinite ($D_{j,i} \to 0$, for example the gas is pure). Actually, the contribution of the compressive advection term in the microcontinuum framework is consistent with that using the standard VOF method [32]. Therefore, compared to the standard CST advection term [17], the compressive advection term can allow for more accurate and flexible simulations of multiscale species transfer, facing the advection- and diffusion-dominated problems.
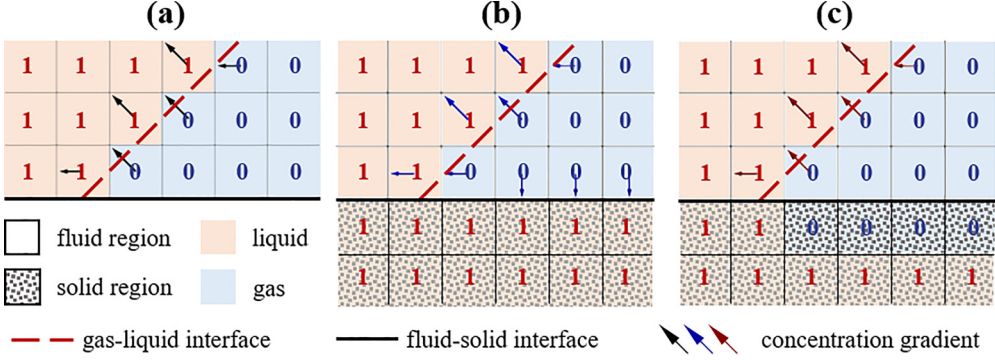
FIG. 1. Graphic representation of the concentration gradient at the solid surface: (a) the pore-scale approach; (b) noncorrected concentration gradient vectors in the multiphase multiscale model; (c) illustration of the concentration extrapolation from the fluid region to the solid region at the fluid/solid interface and the resulting corrected concentration gradient vectors in the multiphase multiscale model.

Following the previous work [30,32], the single-field diffusive term can be derived as

$$\bar{\boldsymbol{J}}_j = -\varepsilon_f \alpha_l D^*_{j,1} \nabla \bar{c}^l_{j,1} - \varepsilon_f \alpha_g D^*_{j,g} \nabla \bar{c}^g_{j,g}$$
$$= -\varepsilon_f \left(D^{m*}_j \nabla \bar{c}_j - \boldsymbol{\Phi}_{\mathrm{CST}} \right), \tag{46}$$

$$D^{m*}_j = \frac{\alpha_l H_j D^*_{j,1} + \alpha_g D^*_{j,g}}{\alpha_l H_j + \alpha_g}, \tag{47}$$

$$\boldsymbol{\Phi}_{\mathrm{CST}} = \frac{(H_j - 1)\bar{c}_j}{\alpha_l H_j + \alpha_g} \nabla \alpha_l, \tag{48}$$

where D^{m*}_j is the weighted mean of the effective diffusion coefficient $D^*_{j,1}$ and $D^*_{j,g}$ in gas and liquid phase weighted by $\alpha_l H_j$ and α_g, and $\boldsymbol{\Phi}_{\mathrm{CST}}$ is the CST flux arising from the concentration jump at the gas-liquid interface. The cornerstone of the CST term is that it transforms the interface condition, Eq. (38), into a volumetric term under the microcontinuum framework.

Eventually, the single-field concentration conservation equation for species j can be reorganized as

$$\frac{\partial \varepsilon_f \bar{c}_j}{\partial t} + \nabla \cdot (\bar{c}_j \bar{\boldsymbol{v}}) + \nabla \cdot \left(\varepsilon_f \frac{(1 - H_j)\bar{c}_j}{\alpha_l H_j + \alpha_g} \alpha_g \alpha_l \boldsymbol{v}_r \right) = \nabla \cdot \left(\varepsilon_f D^{m*}_j (\nabla \bar{c}_j - \boldsymbol{\Phi}_{\mathrm{CST}}) \right) + \dot{n}_j. \tag{49}$$

This equation is referred to hereafter as the multiscale compressive equation (MC-CST), which is distinguished from the standard CST equation without the compressive advection term [17].

The boundary condition for the single-field concentration at the solid wall is given by

$$\varepsilon_f D^{m*}_j (\nabla \bar{c}_j - \boldsymbol{\Phi}_{\mathrm{CST}}) \cdot \boldsymbol{n}_s = 0. \tag{50}$$

Finally, a numerical scheme is used to address the nonphysical concentration gradient problem near the fluid-solid interface (see Fig. 1). In the solid regions, a very small decimal number $\varepsilon_f = 0.01$ was used to replace $\varepsilon_f = 0$ to escape floating-point exceptions [20]. Due to the approximate representation of the solid regions, Eq. (50) cannot completely vanish to zero at the solid wall. To recover the zero-flux boundary condition accurately, gradient terms $\nabla \bar{c}_j$ and $\nabla \alpha_l$ are enforced to zero at the solid wall via the variable extrapolation scheme according to Eqs. (25) and (51). To be more specific, the saturation and concentration of the solid-free region are extrapolated to the nearby

solid region, leading to equal field at either side of the solid wall and the elimination of the gradient terms there,

$$\chi = \begin{cases} 1 & \text{in the macropore and porous region,} \\ 0 & \text{in the solid region,} \end{cases} \quad \chi_f = \text{cell} \lceil \langle \chi \rangle_{c \to f} \rceil,$$

$$\chi_1 = (1 - \chi) \frac{\|\nabla \chi\|}{\|\nabla \chi\| + \delta},$$

$$C_{01} = (\bar{c}_j - \bar{c}_{j,\min})/(\bar{c}_{j,\max} - \bar{c}_{j,\min}),$$

$$C_{01,\text{corr}} = \begin{cases} (1 - \chi_1)C_{01} + \chi_1 \dfrac{\langle \chi_f \langle C_{01} \rangle_{c \to f, \text{harmonic}} \rangle_{f \to c}}{\langle \chi_f \rangle_{f \to c}}, & C_{01,\text{solid}} = 1 \\ 1 - \left((1 - \chi_1)(1 - C_{01}) + \chi_1 \dfrac{\langle \chi_f (1 - C_{01}) \rangle_{c \to f, \text{harmonic}} \rangle_{f \to c}}{\langle \chi_f \rangle_{f \to c}} \right), & C_{01,\text{solid}} = 0 \end{cases}$$

$$\bar{c}_{j,\text{corr}} = C_{01,\text{corr}} \times (\bar{c}_{j,\max} - \bar{c}_{j,\min}) + \bar{c}_{j,\min} \tag{51}$$

where χ is an indicator function representing whether the grid block belongs to the macropore and porous regions or the solid region, χ_1 is an indicator function representing the first layer of grid adjacent to the macropore and porous regions in the solid region, and δ is a very small number to avoid the division to zero, $\lceil \rceil$ denotes the ceiling operator that maps a real number x to the smallest integer greater than or equal to x, $\langle \rangle_{c \to f}$ denotes the interpolation operator from the cell-centered field to the face-centered field, and $\langle \rangle_{f \to c}$ denotes the interpolation operator from the face-centered field to the cell-centered field. The subscript "harmonic" denotes the harmonic-mean scheme used in the interpolation.

III. NUMERICAL METHODS

In this section, numerical implementations to solve partial differential equations for single fields ε_s, α_l, $\bar{p}$, $\bar{\boldsymbol{v}}$, and $\bar{c}_j$ are introduced and discussed, including special solution algorithms, equation discretizations, and numerical workflow.

A. Equation discretization

The solver was developed based on the open-source *multiscalePorousFoam* solver [19] and *GeoChemFoam* solver [38]. The first is implemented for the microcontinuum modeling of the capillary-dominated multiphase flow, while the latter can be used for multiple flow processes, including the multiphase reactive transport with mineral dissolution. The basic computational infrastructure of both comes from the OpenFOAM platform [39–41]. The solver employs the finite volume method (FVM) to solve governing equations on the Eulerian grid, mainly composed of Eqs. (13), (30), (34), (35), and (49). These partial differential equations are first discretized by integrating them over each control volume to yield a set of algebraic equations. During discretization, the first-order *Euler* time scheme is used to discretize the time derivative $\partial/\partial t$ terms. The gradient term ∇ is discretized by the *Gauss linear* scheme, such as $\nabla \bar{p}$ [Eq. (13)] and $\nabla \bar{c}_j$ [Eq. (49)] [19,20]. Advection terms for $\nabla \cdot (\frac{\rho}{\varepsilon_f} \bar{\boldsymbol{v}} \bar{\boldsymbol{v}})$ [Eq. (13)], $\nabla \cdot (\alpha_l \bar{\boldsymbol{v}})$ [Eq. (34)], and $\nabla \cdot (\bar{c}_j \bar{\boldsymbol{v}})$ [Eq. (49)], are performed using the second-order and conservative *Gauss vanLeerV* scheme [42], while compressive terms, including $\nabla \cdot (\varepsilon_f \alpha_l \alpha_g \boldsymbol{v}_r)$ [Eq. (34)] and $\nabla \cdot (\varepsilon_f \frac{(1 - H_j)\bar{c}_j}{\alpha_l H_j + \alpha_g} \alpha_g \alpha_l \boldsymbol{v}_r)$ [Eq. (49)], are implemented by the *interfaceCompression* scheme. The second-order *Gauss linear corrected* scheme is employed to discretize the Laplace term, including $\nabla \cdot (\mu(\nabla \bar{\boldsymbol{v}} + \nabla \bar{\boldsymbol{v}}^T))$ [Eq. (13)] and $\nabla \cdot (\varepsilon_f D_j^{\text{m}*} \nabla \bar{c}_j)$ [Eq. (49)]. For numerical stability, the *Gauss upwinding* scheme is used for the CST term $\nabla \cdot (\boldsymbol{\Phi}_{\text{CST}})$ [Eq. (49)] with respect to the direction of $\pm \nabla \alpha_l$ [36,43].
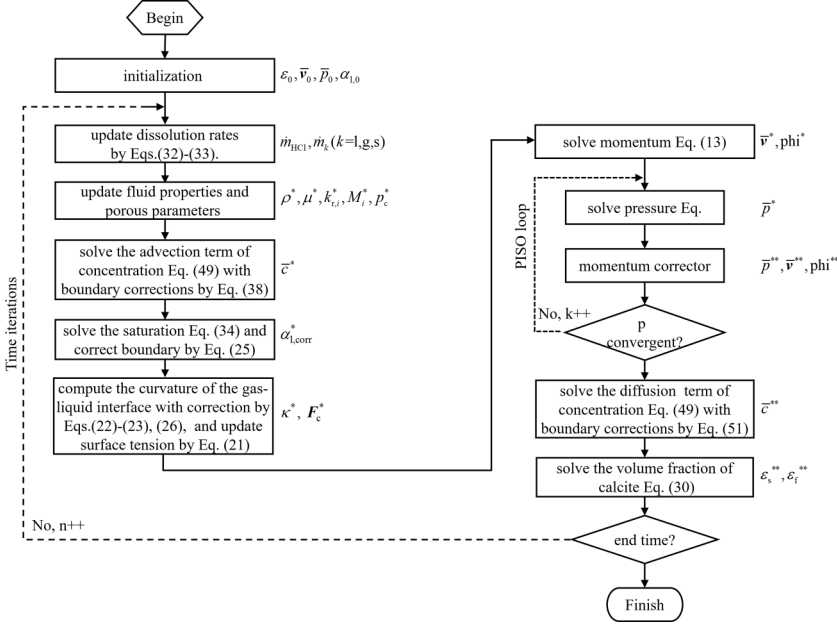
FIG. 2. Flowchart of the microcontinuum model of the multiphase reactive flow.

B. Numerical workflow and solution algorithms

Sequential coupling strategies are performed to iteratively solve the discretized equations of the nonlinear problem at each time step, as illustrated in Fig. 2. By numerical experiments, the time-step size is observed to be controlled by the interface Courant number in the solid-free region, $\mathrm{Co} = \frac{1}{2}\frac{\sum|\phi|}{V}\Delta t$, where ϕ is the mass flux at the gas-liquid interface denoted by $0.01 < \alpha_l < 0.99$. In this work, the interface Courant number is set as 0.01 to limit the spurious velocity to an acceptable magnitude. The main iteration within a time step is depicted as follows.

(1) Calcite dissolution rates $\dot{m}_{\mathrm{HCl}}$ and $\dot{m}_k(k = l, g, s)$ are calculated based on Eqs. (32) and (33) with the concentration and specific reactive surface area from the previous iteration/time step.

(2) The volume fraction of calcite ε_s is explicitly solved by Eq. (30). The local porosity ε_s and its dependent normal vector $\tilde{\boldsymbol{n}}_p^*$ and effective transport properties in the porous matrix, such as the absolute permeability k_0, the effective phase diffusivity $D_{j,i}^*$ and the specific geometric surface area a_v, are updated.

(3) Considering the mass conservation cannot be satisfied unless convergence, the divergent term $\alpha_l \nabla \cdot \bar{\boldsymbol{v}} - \alpha_l \overline{\nabla \cdot \boldsymbol{v}}$ can be introduced at the right-hand side of the saturation equation, Eq. (34), to make up the impact of the numerical flux discontinuity on the saturation boundedness. Along with the mass conservation equation, Eq. (35), the saturation equation can be written as Eq. (52). More detailed derivation is given in Appendix A 2,

$$\frac{\partial \varepsilon_f \alpha_l}{\partial t} + \boldsymbol{\nabla} \cdot (\alpha_l \bar{\boldsymbol{v}}) + \boldsymbol{\nabla} \cdot (\varepsilon_f \alpha_l \alpha_g \boldsymbol{v}_r) = \dot{m}_{\mathrm{HCl}}\frac{\gamma_l}{\rho_l} + \alpha_l\left[\boldsymbol{\nabla}\cdot\bar{\boldsymbol{v}} - \dot{m}_{\mathrm{HCl}}\left(\frac{\gamma_s}{\rho_s} + \frac{\gamma_g}{\rho_g} + \frac{\gamma_l}{\rho_l}\right)\right]. \quad (52)$$

The yielded saturation equation, Eq. (52), is then solved with the explicit source term $\dot{m}_{\mathrm{HCl}}\frac{\gamma_l}{\rho_l}$ and the implicit source term $\alpha_l[\boldsymbol{\nabla}\cdot\bar{\boldsymbol{v}} - \dot{m}_{\mathrm{HCl}}(\frac{\gamma_s}{\rho_s} + \frac{\gamma_g}{\rho_g} + \frac{\gamma_l}{\rho_l})]$ using the multidimensional universal limiter with explicit solution (MULES) algorithm to ensure saturation boundedness [44].

(4) The normal vector $\tilde{\boldsymbol{n}}_{lg}$, the curvature of the gas-liquid interface κ, the surface tension force $\boldsymbol{F}_c$, the capillary pressure p_c, and single-field transport properties (i.e., a_v^l, μk^{-1}, and D_j^{m*}) are updated based on the new saturation field.

(5) The discretized DBS momentum equation, Eq. (13), is then implicitly solved to obtain the predicted velocity $\bar{v}$ and mass flux ϕ, which is so-called the momentum prediction step.

(6) The predicted velocity is corrected based on a predictor-corrector strategy using the splitting of operators (PSIO) algorithms [45], which is so-called the momentum corrector step. For the PISO loop, the semidiscretized pressure equation should be formulated by combining the mass conservation and DBS momentum equations, Eqs. (35) and (13), to take the velocity-pressure coupling into account [15,20]. The pressure equation is then computed and repeated until the convergence of the pressure and velocity fields. The corrector step number of $2 \sim 3$ is recommended to guarantee mass conservation.

(7) The concentration equation, Eq. (49), is solved using the sequential operator splitting algorithm to improve the numerical stability, wherein the advection term is first solved and then injected as a source term in the diffusion equation [43]. At the next iteration, the chemical reaction rate can be updated based on the latest concentration field.

IV. VALIDATION CASES

In this section, four validation cases are implemented to demonstrate the model's applicability and reliability in solving reactive flow and transport across various scales, including pore scale, continuum scale, and hybrid scales. In the first test case, the contribution of the compressive advection term in reducing artificial species transfer at the gas-liquid interface is evaluated by comparing the concentration jump of two-phase flow and transport in a 1D tube using the standard CST term and the compressive CST term to the analytical solutions. The second test case aims to verify the capability of the MC-CST scheme in simulating species transport in a heterogeneous porous medium at the continuum scale. In the third test case, simulations of two-phase flow and transport in capillary tubes are conducted to demonstrate that the saturation/concentration extrapolation scheme can effectively eliminate the artificial advection and diffusion fluxes at the solid boundary and assess the model performance in simulating flow and transport at hybrid scales. Lastly, the microcontinuum model of the multiphase reactive flow is validated by comparing it with Soulaine's experimental results of the dissolution of a calcite crystal in a microchannel [17]. This allows us to assess the model's performance in capturing the dissolution dynamics and its agreement with experimental observations [17]. More information related to the boundary conditions, simulation parameters, and mesh sensitivity analysis is given in the Supplemental Material [46].

A. Two-phase transport in a 1D tube

This test case aims to demonstrate the effectiveness of the MC-CST scheme in mitigating the artificial species transfer at the gas-liquid interface. The standard CST term and the compressive CST term are used to simulate both diffusion-dominated and advection-dominated flow in a 1D tube. The fluid domain extends over $0.2 \, \text{mm} \times 0.01 \, \text{mm}$ and is discretized with a uniform mesh of 400×10 elements. For diffusion-dominated flow, symmetrical boundary conditions are imposed on the top and bottom boundaries for all the variables. The left and right boundaries are subjected to standard no-slip wall conditions, while the diffusion coefficients are set as $D_g = D_l = 10^{-6}$. For advection-dominated flow, liquid is injected from the left boundary with a velocity of 0.05 m/s. Accordingly, the diffusion coefficients are adjusted as $D_g = D_l = 0$, leading to an infinite local Péclet number. Other fluid parameters, such as density and viscosity, remain consistent across all simulations. Especially, the fluid densities and viscosities are $\rho_l = 1000 \, \text{kg/m}^3$, $\rho_g = 20 \, \text{kg/m}^3$, and $\nu_g = \nu_l = 10^{-3} \, \text{m}^2/\text{s}$, respectively. Henry's constant $H = C_l/C_g$ is specified as 2. The surface tension is $\sigma = 0.01 \, \text{kg/s}^2$, while the contact angle on the wall is prescribed as $90°$.

In the case of diffusion-dominated flow, the gas-liquid interface initially resides at the center of the tube, with the liquid phase positioned on the left and the gas phase on the right. The initial concentration of the solute component is $C_l = 0 \, \text{kmol/m}^3$ in the liquid phase and $C_g = 1 \, \text{kmol/m}^3$ in the gas phase. As the solute component diffuses, it undergoes interfacial mass transport from the
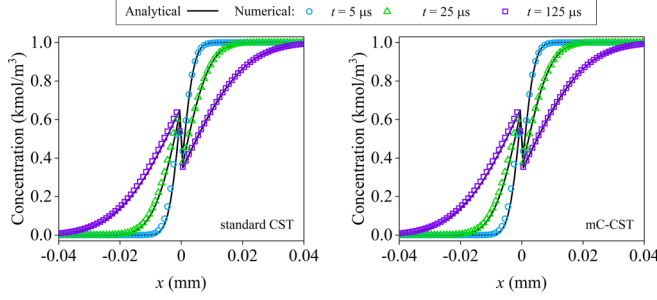
FIG. 3. Comparisons of the analytical solution and numerical results by the standard CST and MC-CST models for the diffusion-dominated flow for very early physical times (zoom in).

gas phase to the liquid phase in order to achieve thermodynamic equilibrium in accordance with Henry's law. Consequently, a concentration jump occurs at the gas-liquid interface. As the spread range of the solute component at the early time is far from the left and right boundaries, the distance between the two planes can be regarded as infinite [47,48]. Based on this assumption, the analytical solution of the concentration field can be derived as [47,48]

$$C(x) = \begin{cases} \beta_0 \text{erf}\left(\frac{\eta_g}{2}\right) + \beta_1, & x > 0 \text{ (in gas phase)}, \\ \gamma_0 \text{erf}\left(\frac{\eta_l}{2}\right) + \gamma_1, & x < 0 \text{ (in liquid phase)}, \end{cases} \tag{53}$$

where $\eta_g = \frac{x}{\sqrt{D_g t}}$, $\eta_l = \frac{x}{\sqrt{D_l t}}$, $\beta_0 = \frac{HC_{g,0} - C_{l,0}}{H + \sqrt{D_l/D_g}}$, $\beta_1 = \frac{\sqrt{D_l/D_g} C_{g,0} + C_{l,0}}{H + \sqrt{D_l/D_g}}$, $\gamma_0 = \sqrt{\frac{D_l}{D_g}} \frac{HC_{g,0} - C_{l,0}}{H + \sqrt{D_l/D_g}}$, and $\gamma_1 = H \frac{\sqrt{D_l/D_g} C_{g,0} + C_{l,0}}{H + \sqrt{D_l/D_g}}$.

For the diffusion-dominated flow, Fig. 3 shows good agreement between the analytical solution and numerical results from both the CST and MC-CST models with the same mean relative errors of 1.22% at 250 μs, as listed in Table I. As expected, the concentration jump can always be guaranteed, which validates the effectiveness of the CST term. Notably, both the CST and MC-CST models are observed to yield almost identical concentration profiles, consistent with the previous work that supports the applicability of the CST model for $\text{Pe}_{\text{local}} < 0.5$ [31].

For the advection-dominated flow, Fig. 4 compares analytical solutions of concentration and saturation profiles and numerical results using CST and MC-CST models at different time, while Fig. 5 illustrates the concentration contour near the gas-liquid interface for the two models. In the absence of interfacial mass transfer, the analytical solutions indicate a sharp front propagating at the liquid injection velocity of 0.05 m/s. However, the CST model smeared the sharp gas-liquid interface due to spurious diffusion at the interface. Conversely, the MC-CST model, upon the introduction of the compressive term, effectively mitigates the spurious diffusion, resulting in a sharp concentration jump that closely aligns with the analytical solutions. Therefore, this test case proves that the proposed MC-CST model within the microcontinuum framework can achieve more accurate and flexible performance to ensure the pore-scale thermodynamic equilibrium condition regardless

TABLE I. The relative error of the simulated Henry's constant $H = C_l/C_g$ at different times for the diffusion-dominated flow.

Time (μs)	25	125	250
$H_{\text{simulated}}$	1.54	1.78	1.90
$H_{\text{analytical}}$	1.44	1.73	1.88
Error	7.01%	2.86%	1.22%
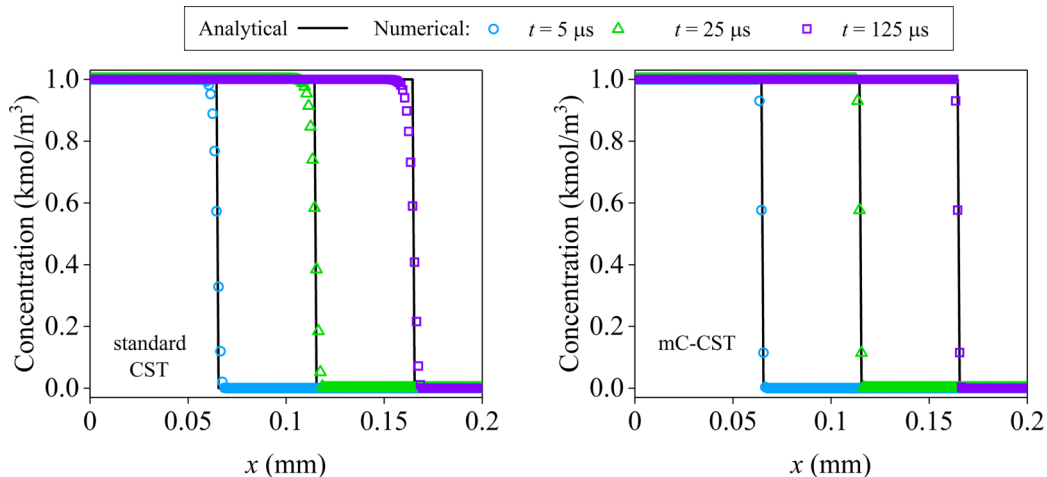
FIG. 4. Comparisons of analytical solutions and numerical results from the standard CST and MC-CST models for the advection-dominated flow case. Solid lines represent the analytical solutions, dashed lines are saturation profiles, and markers depict numerical results.

of diffusion- and advection-dominated scenarios, surpassing the limitations of the previous CST model.

B. Oil drainage and solute transport in a heterogeneous porous medium

To illustrate the applicability of the MC-CST model in solving the multiphase concentration dynamics within complex systems at the Darcy scale, a coupled oil drainage and solute transport process is simulated across a porous medium with spatially heterogeneous permeability. The oil drainage case, originally proposed by Horgue *et al.* [49] and subsequently used by Carrillo *et al.* [15] as a benchmark for validating the multiphase microcontinuum model with the conventional two-phase Darcy model, serves as the foundation for this investigation. Building upon the multiphase microcontinuum model for oil drainage, the MC-CST model is incorporated to substantiate its capability in achieving the thermodynamic concentration equilibrium at the oil-water interface at the Darcy scale. The oil reservoir, measuring 1 by 0.4 m and discretized into a 2000 by 800 grid, is divided into multiple blocks with absolute permeability k_0 values ranging from 1×10^{-13} to 4×10^{-13} m², as shown in Fig. 6. The relative permeabilities within each block are modeled
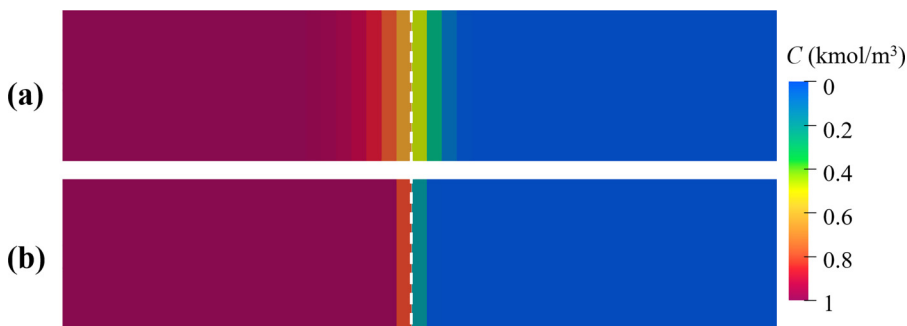
FIG. 5. Concentration contours near the gas-liquid interface for the advection-dominated flow obtained using (a) CST and (b) MC-CST models. The white dashed line is the gas-liquid interface.
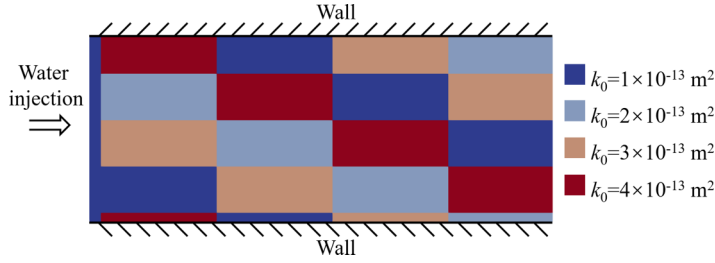
FIG. 6. Darcy-scale simulation configuration of the absolute permeability field and boundary conditions for oil drainage.

through the Van Genuchten model [35], with capillary effects assumed to be negligible. In the simulation, water with a solute concentration of $1\,\text{kmol/m}^3$ is injected from the left boundary at a velocity of $1 \times 10^{-4}\,\text{m/s}$, while the static pressure on the right boundary is maintained at $0\,\text{Pa}$. No-slip wall boundaries with a prescribed contact angle of $90°$ are imposed on the top and bottom boundaries. The fluid densities and viscosities are $\rho_{\text{water}} = 1000\,\text{kg/m}^3$ and $\rho_{\text{oil}} = 800\,\text{kg/m}^3$, $\nu_{\text{water}} = 10^{-6}\,\text{m}^2/\text{s}$, and $\nu_{\text{oil}} = 1.25 \times 10^{-4}\,\text{m}^2/\text{s}$, respectively. The surface tension is set as $\sigma = 0.15\,\text{kg/s}^2$. The solute diffusion coefficients are specified as $D_{\text{oil}} = D_{\text{water}} = 10^{-5}\,\text{m}^2/\text{s}$, and Henry's constant $H = C_{\text{water}}/C_{\text{oil}}$ varies as 1, 2, and 5.

Figure 7 shows that viscous fingering instabilities appear on the water saturation front, consistent with previous Carrillo et al.'s simulations [15]. Figure 8 compares temporal concentration distributions solved using various Henry's constants. When $H = 1$, the concentration field is continuous between oil and water phases without the concentration jump, wherein the solute transport is predominantly influenced by both advection and diffusion mechanisms. As H increases from 1 to 5, the CST term progressively establishes a concentration jump at the oil-water interface, resulting in a decrease in concentration within the oil phase. Figure 9 shows the concentration ratio $H_{\text{calc}} = C_{\text{water}}/C_{\text{oil}}$ at the oil-water interface closely approximating the prescribed Henry constant, with relative errors less than 1% at 100 s. This case convincingly demonstrates the capability of the MC-CST equation in accurately simulating species transport within a heterogeneous porous medium at the Darcy scale.
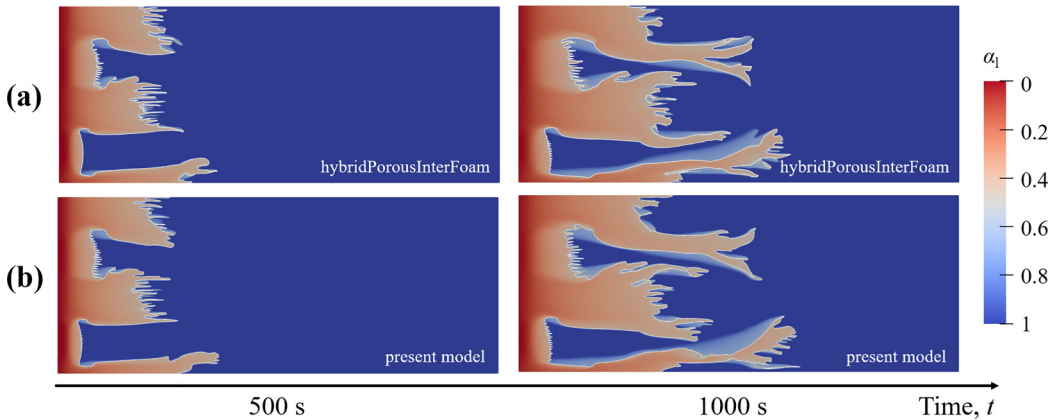
FIG. 7. Simulation results of liquid saturation solved by (a) hybridPorousInterFoam, and (b) the present model. The white line delineates the oil-water interface.
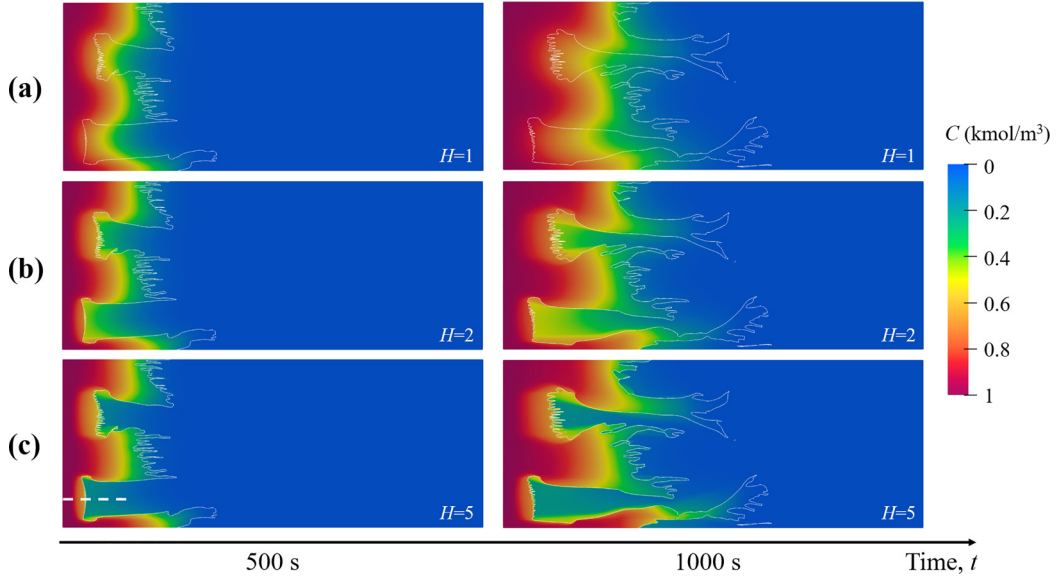
FIG. 8. Simulation results of solute concentration solved by the present model for different Henry's constant: (a) $H = 1$, (b) $H = 2$, (c) $H = 5$. The white line delineates the oil-water interface.

C. Capillary flow and transport at hybrid scale

This test case aims to validate the capability of the improved microcontinuum model in simulating the two-phase flow and transport at the hybrid scale. As shown in Figs. 10(a) and 11(a), two narrow tubes are considered: one with fluid and solid regions, and the other with fluid, porous, and solid regions, to validate the capability of the MC-CST equation to accurately model the transport process of two-phase flow in hybrid scale. The computational fluid domain extends over $10 \, \text{mm} \times 2 \, \text{mm}$ and is discretized using a uniform mesh of 400×80 elements. Within the domain, solid and porous blocks measuring $8 \, \text{mm} \times 2 \, \text{mm}$ are inserted and positioned at the top and bottom, respectively, leaving solid-free flow buffer regions of $1 \, \text{mm}$ width at the entrance and exit. The impermeable solid region is approximated by a porosity of $\varepsilon_f = 10^{-3}$ and a Kozeny-Carman coefficient of $k_c = 10^{-16} \, \text{m}^2$, while the porous matrix is characterized by a porosity of $\varepsilon_f = 0.3$ and a Kozeny-Carman coefficient of $k_c = 10^{-14} \, \text{m}^2$. The absolute permeability varies from the local
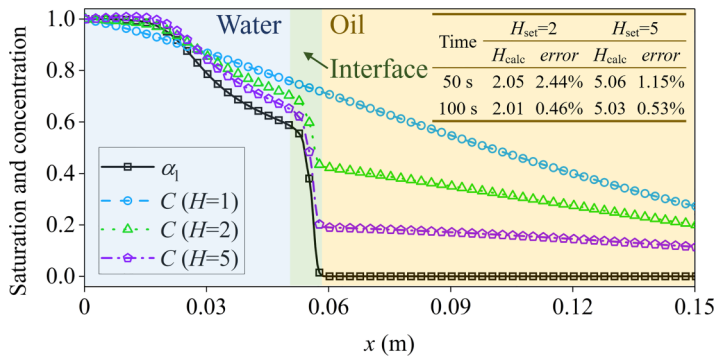
FIG. 9. Simulated concentration profile along the horizontal line at $y = 0.06 \, \text{m}$ for different Henry's constants. The horizontal line is labeled in Fig. 8(c).
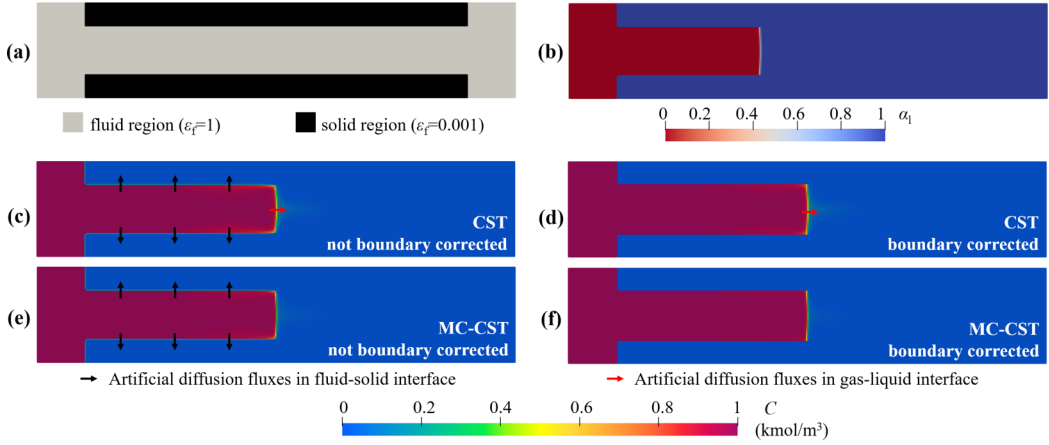
FIG. 10. Simulation domain and results of the solid tube case: (a) domain configuration, (b) liquid saturation field ($t = 0.3$ s), and concentration fields ($t = 0.3$ s) solved using (c) the CST model without boundary correction, (d) the CST model with boundary correction, (e) the MC-CST model without boundary correction, and (f) the MC-CST model with boundary correction.

porosity based on the Kozeny-Carman relation. Symmetrical boundary conditions are applied to the top and bottom boundaries for all the variables. At the left boundary, liquid with a solute concentration of $1\,\text{kmol/m}^3$ is injected at a velocity of 5×10^{-3} m/s, while the right boundary maintains a static pressure of 0 Pa. The fluid densities and viscosities are set as $\rho_l = 1000\,\text{kg/m}^3$ and $\rho_g = 50\,\text{kg/m}^3$, $\nu_l = 10^{-6}$, and $\nu_g = 1.48 \times 10^{-5}\,\text{m}^2/\text{s}$, respectively. The surface tension is $\sigma = 0.001\,\text{kg/s}^2$, while the contact angle on the solid/porous boundary is prescribed as $90°$. The solute diffusion coefficients are $D_g = D_l = 10^{-8}\,\text{m}^2/\text{s}$, and Henry's constant $H = C_l/C_g$ varies as 1, 2, 5, and 10.

Initially, we focus on validating the effectiveness of the compressive CST term and the boundary correction using a variable extrapolation scheme on mitigating artificial species transfer at the gas-liquid interface and the fluid-solid interface, respectively. As observed in Fig. 10(b), the injected liquid displaces the gas phase within the fluid tube, resulting in a distinct fluid-solid interface and
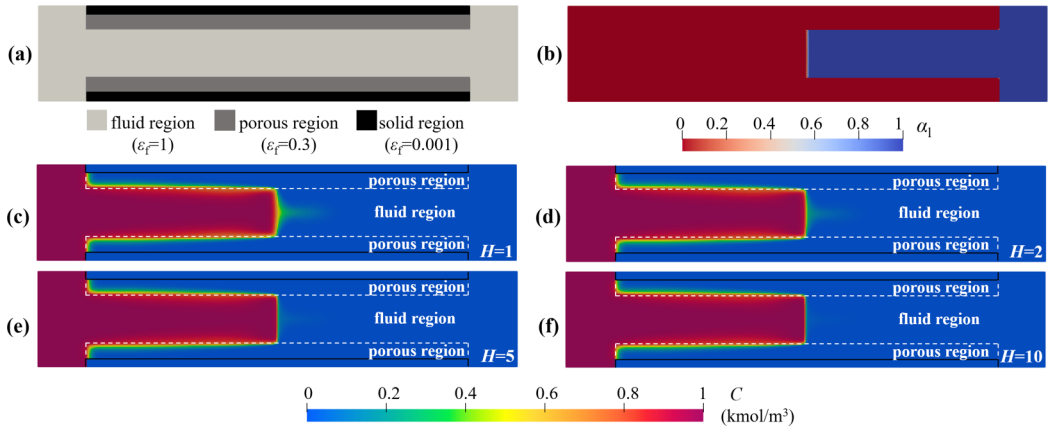
FIG. 11. Simulation domain and results of the porous tube case: (a) domain configuration, (b) liquid saturation field ($t = 0.3$ s), and concentration fields ($t = 0.3$ s) solved by the MC-CST model with various Henry's constants of (c) $H = 1$, (d) $H = 2$, (e) $H = 5$, and (f) $H = 10$.

sharp gas-liquid interface. However, both Figs. 10(c) and 10(e) indicate that numerical diffusion blurs the sharp concentration jump at the impermeable solid boundary when the boundary correction scheme is not implemented. This behavior arises due to the approximation of the solid regions by $\varepsilon_f = 0.01$ and the presence of a substantial concentration gradient at the fluid-solid region, which then generates artificial diffusion fluxes and breaks the impermeable solid boundary condition. By incorporating the variable extrapolation scheme, the concentration gradient at the solid boundary is enforced to zero. Figures 10(d) and 10(f) illustrate the effective elimination of artificial diffusion fluxes, rendering the fluid-solid interface equivalent to zero-gradient wall boundaries as described by Eq. (50). Furthermore, as the solute transport is dominated by advection ($Pe_{local} = 12\,500$), artificial advection fluxes emerge at the gas-liquid interface solving by the CST model shown in Figs. 10(c) and 10(d). Similar to Case B, the additional compressive term in the MC-CST model successfully mitigates these artificial advection fluxes, thereby preserving a sharp gas-liquid interface during the advection-dominated transport, as shown in Fig. 10(f).

After validating the effectiveness of the compressive CST term and the boundary correction, a porous region is introduced for the assessment of the improved microcontinuum model's performance at the fluid-porous interface, as shown in Fig. 11. Initially, the porous region is fully saturated with the liquid phase for the exclusive occurrence of gas drainage within the fluid tube. In the case of the Henry's constant of 1, the concentration is continuous at the gas-liquid interface shown in Fig. 11(c). Notably, the solute transport along the central axis of the tube is accelerated due to the parabolic velocity profile perpendicular to the flow direction. The solute gradually diffuses into the adjacent porous matrix as it progresses with the flow, which is consistent with the reported solute diffusion observed in altered porous layers surrounding fracture surfaces [25,50]. As the Henry's constant increases, the interfacial mass transport becomes progressively restricted due to the changed thermodynamic equilibrium condition at the gas-liquid interface. Overall, this test case proves the model's capacity to successfully simulate flow and transport under high Péclet number condition at the hybrid scale.

D. Multiphase dissolution of a calcite grain

In the last test case, the simulation of multiphase reactive flow and transport is validated against Soulaine's experiments regarding the dissolution of a calcite grain in a microchannel [17]. The computational domain is a $1.5\,mm \times 1.5\,mm$ two-dimensional box which contains a round calcite grain with a diameter of $0.5\,mm$ positioned at the center. The calcite grain is a solid characterized by a porosity of $\varepsilon_f = 10^{-3}$ and a Kozeny-Carman coefficient of $k_c = 10^{-15}\,m^2$. The absolute permeability varies from the local porosity based on the Kozeny-Carman relation. A uniform mesh of 100×100 elements is utilized to discretize the domain. No-slip wall boundaries with no reaction are imposed on the top and bottom boundaries. Liquid with a solute concentration of $0.1\,kmol/m^3$ is injected from the left boundary at a velocity of $5.8 \times 10^{-4}\,m/s$, while the static pressure on the right boundary is set to 0 Pa. The fluid densities and viscosities are $\rho_l = 1000\,kg/m^3$ and $\rho_g = 1\,kg/m^3$, $v_l = 10^{-6}$, and $v_g = 1 \times 10^{-3}\,m^2/s$, respectively. The surface tension is $\sigma = 0.001\,kg/s^2$, and the contact angle on the calcite particle is prescribed as $45°$. The solute diffusion coefficients are $D_g = D_l = 5 \times 10^{-9}\,m^2/s$, and the Henry's constant $H = C_l/C_g$ is specified as 2.

Figure 12 captures the temporal two-phase dissolution of the solid calcite grain. CO_2 gas is produced at the grain surface, leading to gas bubbles driven by surface tension forces. Consistent with experimental observations conducted by Soulaine et al. [17], the simulation shows that the small gas bubbles grow and coalesce with their closest neighbors, resulting in the formation of several larger bubbles that display a relatively uniform distribution around the grain. These large bubbles swing in response to the flow and eventually detach from the surface after reaching a critical size. This cyclic sequence of growth, coalescence and detachment repeats throughout the calcite dissolution. Notably, the presence of gas bubbles hinders direct contact between some calcite surfaces and the acidic liquid, resulting in a reduced reactive surface area and a slower dissolution rate. Therefore, a small shrinkage of the calcite grain can be visualized within 180 s.
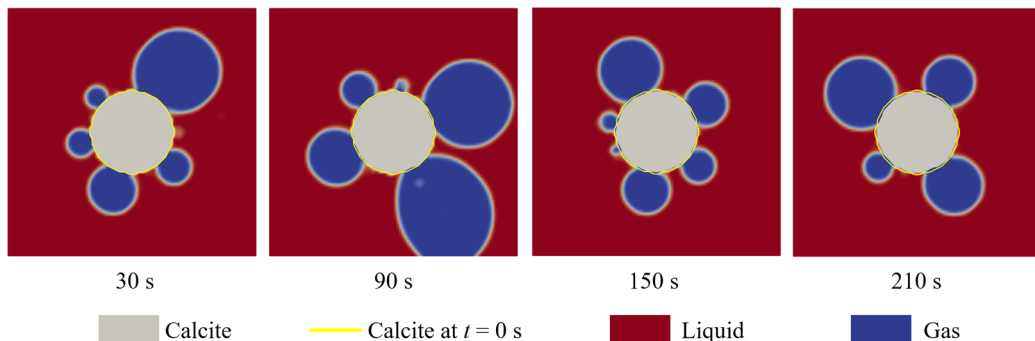
FIG. 12. Simulation results for temporal evolutions of fluid saturation and calcite structure during the multiphase dissolution.

Figure 13 compares the evolution of the normalized calcite mass between numerical simulations and experimental measurements [17]. The normalized calcite mass is computed by integrating the volume fraction of the solid phase and normalizing it by its initial value as

$$m_{\text{calcite}}^*(t) = \frac{\int_V \varepsilon_s(t)dV}{\int_V \varepsilon_s(0)dV}. \tag{54}$$

Generally, the simulation result shows some agreements with experimental measurements [17], with a mean relative error of 2.2% in the last 30 s. However, it should be noted that the simulation slightly overpredicts the dissolution rate at the beginning. This discrepancy could potentially be attributed to the model's relatively low surface tension and the absence of top and bottom wall adhesion effects, which could lead to a higher frequency of gas bubble detachment in the 2D simulations [17].

V. APPLICATION CASE

In this section, the improved microcontinuum model is employed to investigate the multiphase reactive flow and transport during acidic liquid injection into a multiscale porous medium. Particularly, this simulation focuses on understanding the effects of subgrid porosity within the
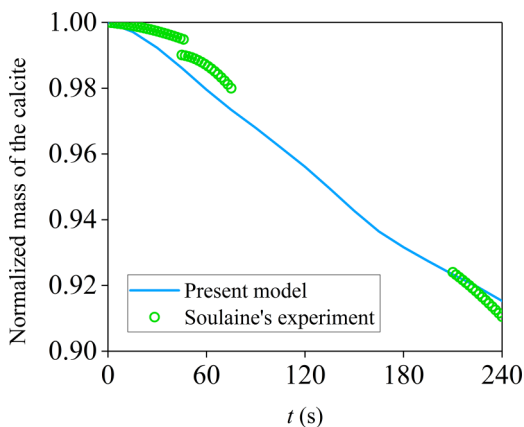
FIG. 13. Comparisons of the residual normalized mass of the calcite grain between numerical results and experimental measurement [17].
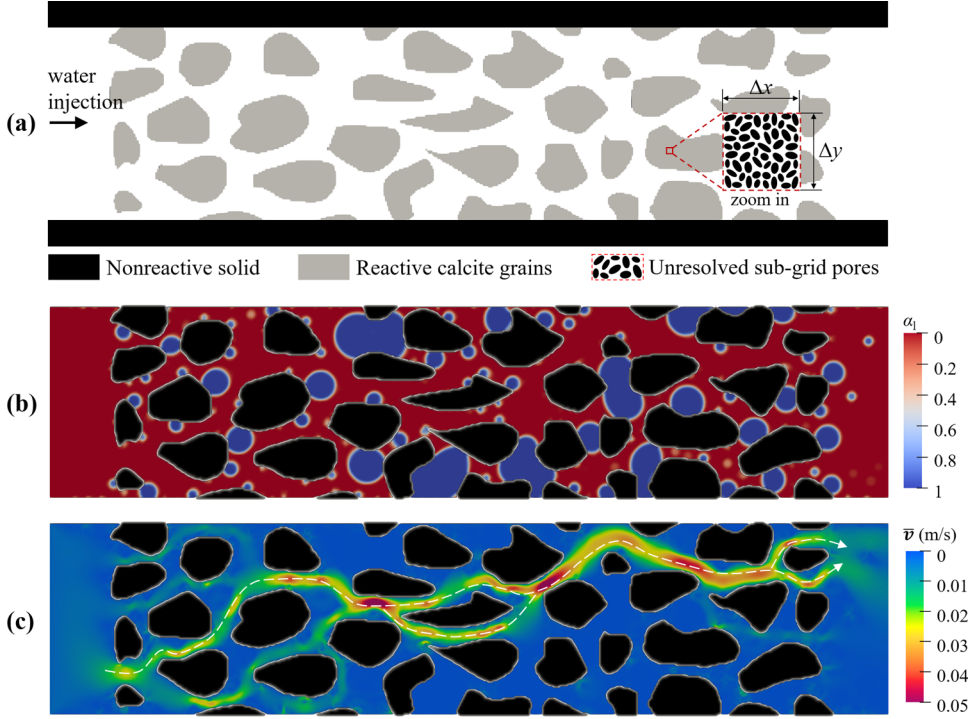
FIG. 14. Snapshots of (a) computational domain, (b) liquid saturation, and (c) velocity magnitude fields at $t = 20$ s solved for the multiphase dissolution of solid grains. Black irregular particles represent the solid calcite grains, while the white solid line delineates the fluid-solid interface ($\varepsilon_f = 0.85$ isosurface). The white dashed line delineates the preferential flow pathway.

subresolution porous calcite matrix on the multiphase dissolution dynamics. As shown in Fig. 14(a), the computational domain is 1000 μm × 290 μm in size and is meshed using a 500 × 145 Cartesian grid. Nonslip wall conditions are imposed by introducing solid regions of 1000 μm × 30 μm at the top and bottom boundaries. The central region of the domain, measuring 960 μm × 230 μm, represents the pore-scale porous medium comprising irregular calcite grains. The average size of resolved macropores is around 50 μm. These calcite grains can exist as impermeable solid structures or as porous matrices containing subgrid pores. The impermeable solid calcite grains are approximated by a porosity of 0.001 and a Kozeny-Carman coefficient of $k_c = 10^{-16}$ m^2, while the porous calcite grains are characterized by a porosity ranging from 0.1 to 0.3 and a Kozeny-Carman coefficient of $k_c = 10^{-13}$ m^2. The absolute permeability varies from the local porosity based on the Kozeny-Carman relation. Initially, the computational domain is fully saturated with gas denoted as "g." To simulate the dissolution of calcite grains, a hydrochloric acid solution with a concentration of 0.15 kmol/m^3, denoted as "l," is injected from the left inlet with a velocity of 0.003 m/s. The fluid densities and viscosities are $\rho_l = 1000$ kg/m^3 and $\rho_g = 100$ kg/m^3, $\nu_l = 10^{-6}$ m^2/s, and $\nu_g = 10^{-4}$ m^2/s, respectively. The surface tension is $\sigma = 0.005$ kg/s^2, and the contact angle on the calcite particle is prescribed as 45°. The solute diffusion coefficients are $D_g = 5 \times 10^{-7}$ m^2/s and $D_l = 10^{-8}$ m^2/s, and the Henry's constant $H = C_l/C_g$ is 10. The reaction constant is set as $r = 5 \times 10^{-3}$ m/s. The temporal evolution of the sub-grid-specific geometrical area inside the porous calcite grains is modeled using the sugar-lump model [51].

Figures 14(b) and 14(c) illustrate the liquid saturation field and velocity magnitude field at the time of 20 s for the multiphase dissolution of solid grains. The dissolution of calcite results in the generation of CO$_2$ gas, which subsequently grows and merges to form multiple large bubbles. These
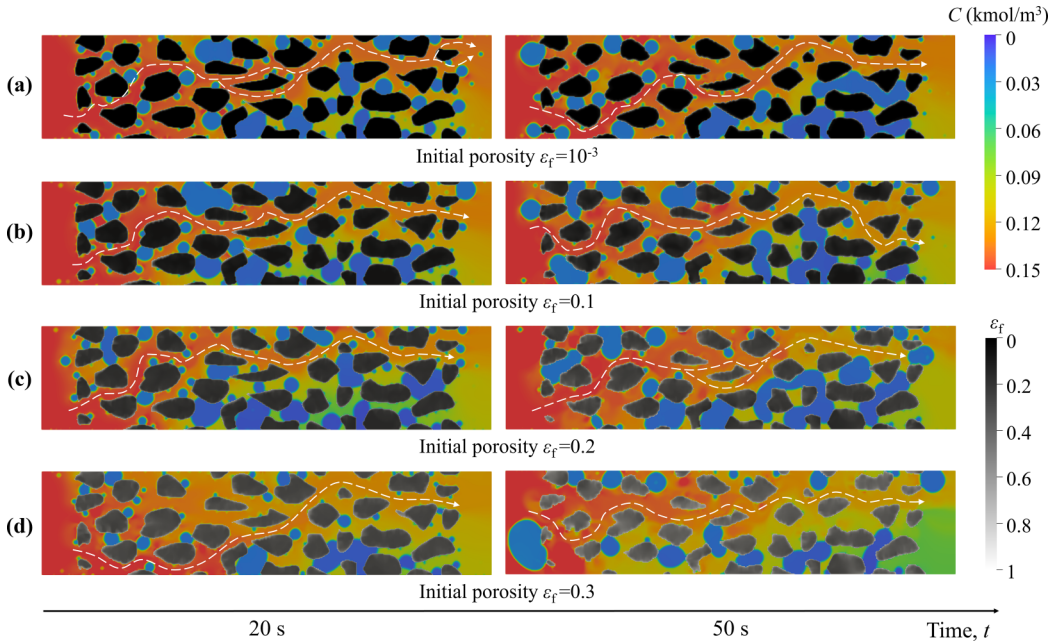
FIG. 15. Snapshots of concentration fields at $t = 20$ and 50 s in fluid regions for the multiphase dissolution of (a) solid grains, and porous grains with porosity of (b) $\varepsilon_f = 0.1$, (c) $\varepsilon_f = 0.2$, and (d) $\varepsilon_f = 0.3$. The white dashed line delineates the preferential flow pathway. The color ranging from white to black within the solid grains corresponds to the volume fraction of the solid phase, varying from 0 to 1.

large CO_2 bubbles, influenced by surface tension and wall adhesion conditions, become trapped in certain pore spaces and act as flow barriers. The presence of fewer and smaller bubbles in specific pores and throats creates a preferential flow pathway for the injected solution, spanning from the bottom left to the top right within the computational domain. This preferential flow path significantly influences the distribution of acid concentration and, consequently, the evolution of the calcite structure, as depicted in Figs. 15(a) and 16(a). Grains located along the preferential path experience accelerated dissolution rates compared to those located elsewhere. This phenomenon can be attributed to the efficacious replenishment of consumed hydrochloric acid by the inflowing solution, leading to higher acid concentrations in the fluid vicinity of these grains shown in Fig. 15(a). Additionally, the porous layer formed around the surface of solid grains also present elevated acid concentration, as evidenced in Fig. 16(a). Furthermore, the higher flow velocity facilitates the detachment and removal of gas bubbles from the grain surface, thereby increasing the reactive surface. The combined effects of the higher acid concentration and expanded reactive surface area can intensify the dissolution along the preferential path. Conversely, gas bubbles formed on the surface of grains outside the preferential path tend to grow and envelop the grain, hindering subsequent transport and dissolution processes. Overall, the multiphase dissolution across the single-scale porous medium packed by solid calcite grains exhibits a typical wormholing pattern.

Figures 15(b)–15(d) and Figs. 16(b)–16(d) compare the concentration distribution and structural evolution of the porous calcite grains with various subgrid porosities. In contrast to the dissolution occurring solely at the fluid-solid interface for solid grains, the infiltration of the solution into the porous grains leads to an increased reactive surface area and, consequently, an accelerated dissolution rate. Figure 17 shows that the dissolution rate further rises with the increasing subgrid porosity. The normalized mass of calcite is calculated as Eq. (54). At $t = 50$ s, the normalized dissolution mass of porous calcite grains with subgrid porosities of 0.1, 0.2, and 0.3 is found to be
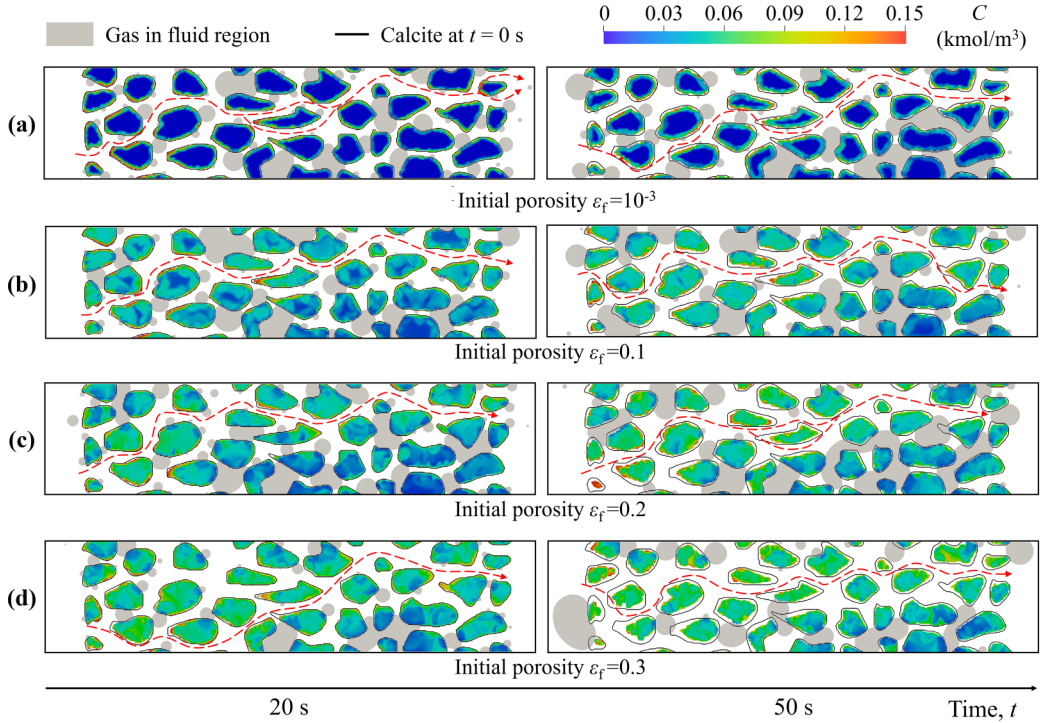
FIG. 16. Snapshots of concentration fields at $t = 20$ and 50 s within solid and porous regions for the multiphase dissolution of (a) solid grains, and porous grains with porosity of (b) $\varepsilon_f = 0.1$, (c) $\varepsilon_f = 0.2$, and (d) $\varepsilon_f = 0.3$. The red dashed line delineates the preferential flow pathway. The white represents the fluid regions, and the gray area represents the gas phase. The black solid line represents calcite at $t = 0$ s.

1.7, 2.2, and 3.1 times higher than that of solid calcite grains, respectively. Accordingly, the highest dissolution rate occurs in the multiphase dissolution of the porous grains with the subresolution porosity of $\varepsilon_f = 0.3$ among all the simulations. In this particular scenario, Fig. 15(d) illustrates the presence of an acid concentration gradient along the flow direction, resulting in a slower dissolution
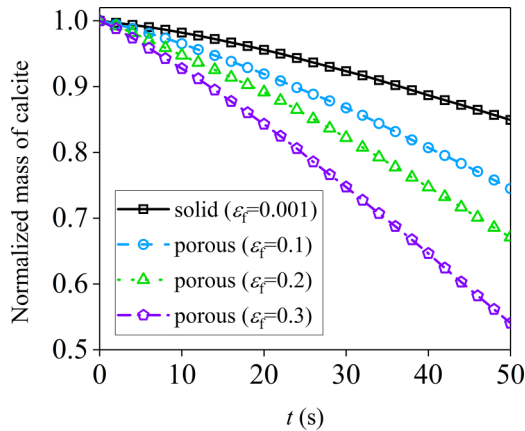
FIG. 17. Normalized mass of solid grains and porous grains with the porosity of $\varepsilon_f = 0.1, 0.2, 0.3$. The capillary effect in the subresolution porous medium is not considered.
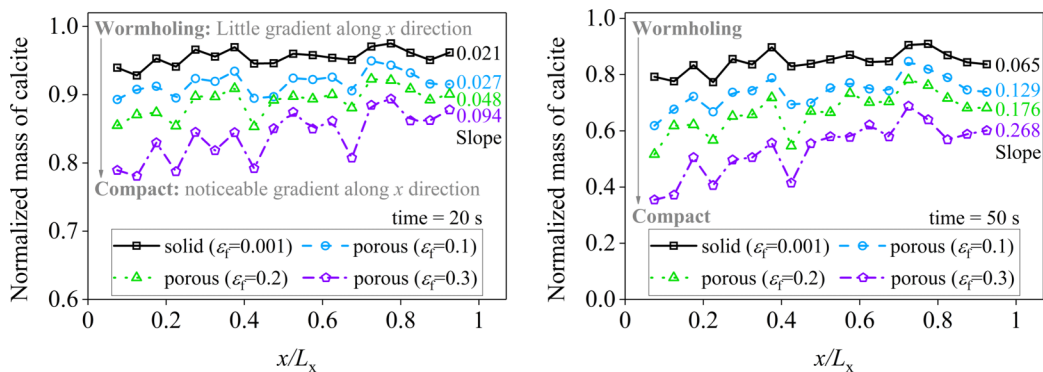
FIG. 18. Profiles of normalized mass along the x direction at 20 and 50 s of solid grains and porous grains with a porosity of $\varepsilon_f = 0.1, 0.2, 0.3$. The slope is calculated by linear regression of the normalized mass of calcite and the dimensionless length of the x direction.

rate for downstream grains in comparison to upstream grains. Moreover, the formation of large bubbles is not limited to areas outside the initially preferential flow path and can be observed in upstream regions where rapid dissolution occurs, as shown in Fig. 16(d). Quantitative analysis of the normalized mass of calcite along the flow direction was conducted to discern the dissolution patterns, as depicted in Fig. 18. The results reveal a uniform distribution of the normalized mass of the solid grain along the x direction, indicative of a wormhole dissolution pattern. However, as the initial porosity increases, noticeable gradients in the normalized mass of the porous grains are observed along the x direction. Specifically, at $t = 50$ s, the slopes of the normalized mass for the porous grains with porosities are found to be 2, 2.7, and 4.1 times higher than those of the solid grains, respectively. Therefore, the altered temporal evolution of calcite structures and spatial distribution of large CO_2 bubbles suggest a transition from a wormhole dissolution pattern to a more compact dissolution pattern.

In summary, this application showcase demonstrates the capability of the improved micro-continuum model to accurately simulate the multiscale dissolution dynamics, incorporating the interplay of multiphase reactive flow and transport at both the pore scale (resolved pores) and Darcy scale (unresolved pores). The simulation results emphasize the significance of considering multiscale fluid-rock interactions in image-based modeling of mineral dissolution, particularly in capturing the dissolution regime accurately. This is crucial due to the presence of subresolution pores in micro-CT images caused by the inherent limitations in spatial resolution. It is worth noting that the computational efficiency of the multiphase microcontinuum model still requires further improvement to enable longer simulations and capture more significant calcite dissolution. This is due to the necessity of using small time steps and maintaining a Courant number below 0.01 to mitigate spurious velocity magnitudes at the contact line, particularly after the physical time of 10 s for this application case. Therefore, the development of advanced numerical schemes and algorithms is essential to enhance the practicality of the multiphase microcontinuum model.

VI. CONCLUSIONS

The study has improved the multiphase microcontinuum model for accurately and flexibly simulating the multiscale multiphase reactive flow and transport during mineral dissolution. Rigorous derivations of single-field advection and diffusion fluxes are performed using volume-averaging principles applied to the species transfer equation. The multiscale compressive continuum species transfer (MCCST or MC-CST) model is derived by including an additional compressive term. This modification effectively addresses the issue of numerical diffusion at the gas-liquid interface encountered in the previous microcontinuum CST model. Additionally, to account for spurious

species transfer at the fluid-solid interface resulting from the approximate representation of the solid region in the microcontinuum framework, a concentration extrapolation algorithm is proposed to ensure the impermeable wall condition. By coupling the single-field solid/fluid mass, momentum, and saturation equations with appropriate subgrid models such as the sugar-lump reactive surface area model, the improved multiphase microcontinuum model enables the simulation of mineral dissolution considering spatially multiscale fluid-rock interactions and temporal structural evolution. Notably, the enhanced microcontinuum model possesses a multiscale capability, resembling a volume of fluid (VOF) -based Navier-Stokes model at the pore scale for resolved macropores/fractures, and a two-phase Darcy model at the continuum scale for unresolved micropores.

To assess the numerical performance of the improved microcontinuum model across various scales, four validation cases are conducted, including the pore scale, Darcy scale, and hybrid scales. First, the multiscale compressive CST model is validated by simulating pore-scale two-transport phenomena in a 1D tube. The results demonstrate the model's ability to mitigate artificial species transfer and maintain thermodynamic equilibrium at the gas-liquid interface for advection-dominated transport. Second, oil drainage and solute transport across a heterogeneous porous medium are simulated to demonstrate the model's capability in simulating the Darcy-scale problem. Third, simulations of two-phase flow and transport in capillary tubes containing a porous matrix are conducted to demonstrate that the numerical model can handle the flow and transport under high Péclet number conditions at the hybrid scales. Lastly, the impact of CO_2 gas bubble dynamics on multiphase dissolution is investigated through the simulation of single solid calcite dissolution. The satisfactory agreement between the simulation results and experimental data validates the capacity of the models to capture multiphase reactive flow and transport phenomena.

After the validation, an application case is conducted by simulating the multiphase dissolution of calcite grains in both single-scale and multiscale porous media. In the single-scale porous medium, a distinct wormholing dissociation pattern is observed, which can be attributed to the presence of flow barriers caused by large CO_2 gas bubbles and the establishment of a preferential pathway for two-phase flow. However, when considering the subgrid reactive transport within the highly porous calcite grains, the dissolution pattern gradually transitions into a more compact pattern. This transformation is primarily driven by an increased dissolution rate at the upstream flow region due to the larger reactive surface area. This application case suggests the significance of accurately modeling the multiscale fluid-rock interaction for predicting and understanding dissolution patterns.

In future work, there is a need to enhance the multiphase microcontinuum model. Efforts should be focused on reducing the occurrence of spurious velocity when considering the significant capillary forces present in the subresolution micro- or even nanopores. In the meantime, the computational efficiency of the model should be further enhanced to enable simulations of mineral dissolution in complex porous media with larger computational domains, longer physical time scales, and natural geological structures. These advancements will contribute to more realistic and comprehensive simulations of natural mineral dissolution processes.

APPENDIX: DERIVATION OF THE COMPRESSIVE ADVECTION TERM AND SOURCE TERMS IN THE SATURATION EQUATION

1. Compressive advection term

This Appendix derives the compressive advection term of the single-field concentration conservation equation from the volume-averaged concentration equations for the gas and liquid phases as

Eq. (43). To replace the phase-averaged variables in the advection term $\nabla \cdot (\varepsilon_f \alpha_l \bar{c}_{j,1}^l \bar{v}_l^l + \varepsilon_f \alpha_g \bar{c}_{j,g}^g \bar{v}_g^g)$ with the single-field variables, the above two items are expressed using Eq. (2) as

$$\varepsilon_f \alpha_l \bar{c}_{j,1}^l \bar{v}_l^l = \bar{c}_{j,1}^l \bar{v} - \varepsilon_f \alpha_g \bar{c}_{j,1}^l \bar{v}_g^g, \quad \varepsilon_f \alpha_g \bar{c}_{j,g}^g \bar{v}_g^g = \bar{c}_{j,g}^g \bar{v} - \varepsilon_f \alpha_l \bar{c}_{j,g}^g \bar{v}_l^l. \tag{A1}$$

Add the two items and organize to get

$$\varepsilon_f \alpha_l \bar{c}_{j,1}^l \bar{v}_l^l + \varepsilon_f \alpha_g \bar{c}_{j,g}^g \bar{v}_g^g = \left(\bar{c}_{j,1}^l \bar{v} + \bar{c}_{j,g}^g \bar{v} \right) - \left(\varepsilon_f \alpha_g \bar{c}_{j,1}^l \bar{v}_g^g + \varepsilon_f \alpha_l \bar{c}_{j,g}^g \bar{v}_l^l \right). \tag{A2}$$

The first and second items on the right side of Eq. (A2) are multiplied by $\alpha_l + \alpha_g = 1$ and merged using Eqs. (2) and (3),

$$\begin{aligned} \bar{c}_{j,1}^l \bar{v} + \bar{c}_{j,g}^g \bar{v} &= \left[(\alpha_l + \alpha_g) \bar{c}_{j,1}^l \bar{v} + (\alpha_l + \alpha_g) \bar{c}_{j,g}^g \bar{v} \right] \\ &= \left(\alpha_l \bar{c}_{j,1}^l \bar{v} + \alpha_g \bar{c}_{j,g}^g \bar{v} \right) + \left(\alpha_g \bar{c}_{j,1}^l \bar{v} + \alpha_l \bar{c}_{j,g}^g \bar{v} \right) \\ &= \bar{c}_j \bar{v} + \alpha_g \bar{c}_{j,1}^l \left(\varepsilon_f \alpha_g \bar{v}_g^g + \varepsilon_f \alpha_l \bar{v}_l^l \right) + \alpha_l \bar{c}_g^g \left(\varepsilon_f \alpha_g \bar{v}_g^g + \varepsilon_f \alpha_l \bar{v}_l^l \right). \end{aligned} \tag{A3}$$

Use Eqs. (A3) into (A2), and rewrite $\alpha_g \alpha_g$ and $\alpha_l \alpha_l$ to $\alpha_g (1 - \alpha_l)$ and $\alpha_l (1 - \alpha_g)$, respectively. Cancel the liked items to express the advection term by the single-field velocity and the relative velocity as

$$\begin{aligned} \varepsilon_f \alpha_l \bar{c}_{j,1}^l \bar{v}_1^1 + \varepsilon_f \alpha_g \bar{c}_{j,g}^g \bar{v}_g^g &= \bar{c}_j \bar{v} + \left(\varepsilon_f \alpha_g \alpha_l \bar{c}_{j,1}^l \bar{v}_1^1 + \varepsilon_f \alpha_g \alpha_l \bar{c}_{j,g}^g \bar{v}_g^g \right) \\ &\quad + \left(\varepsilon_f \alpha_g \alpha_g \bar{c}_{j,1}^l \bar{v}_g^g + \varepsilon_f \alpha_l \alpha_l \bar{c}_{j,g}^g \bar{v}_1^1 \right) - \left(\varepsilon_f \alpha_g \bar{c}_{j,1}^l \bar{v}_g^g + \varepsilon_f \alpha_l \bar{c}_{j,g}^g \bar{v}_1^1 \right) \\ &= \bar{c}_j \bar{v} + \left(\varepsilon_f \alpha_g \alpha_l \bar{c}_{j,1}^l \bar{v}_1^1 + \varepsilon_f \alpha_g \alpha_l \bar{c}_{j,g}^g \bar{v}_g^g \right) \\ &\quad + \left(\varepsilon_f \alpha_g (1 - \alpha_l) \bar{c}_{j,1}^l \bar{v}_g^g + \varepsilon_f \alpha_l (1 - \alpha_g) \bar{c}_{j,g}^g \bar{v}_1^1 \right) - \left(\varepsilon_f \alpha_g \bar{c}_{j,1}^l \bar{v}_g^g + \varepsilon_f \alpha_l \bar{c}_{j,g}^g \bar{v}_1^1 \right) \\ &= \bar{c}_j \bar{v} + \left(\varepsilon_f \alpha_g \alpha_l \bar{c}_{j,1}^l \bar{v}_1^1 + \varepsilon_f \alpha_g \alpha_l \bar{c}_{j,g}^g \bar{v}_g^g \right) \\ &\quad + \left(\varepsilon_f \alpha_g (1 - \alpha_l) \bar{c}_{j,1}^l \bar{v}_g^g + \varepsilon_f \alpha_l (1 - \alpha_g) \bar{c}_{j,g}^g \bar{v}_1^1 \right) - \left(\varepsilon_f \alpha_g \bar{c}_{j,1}^l \bar{v}_g^g + \varepsilon_f \alpha_l \bar{c}_{j,g}^g \bar{v}_1^1 \right) \\ &= \bar{c}_j \bar{v} + \left(\varepsilon_f \alpha_g \alpha_l \bar{c}_{j,1}^l \bar{v}_1^1 + \varepsilon_f \alpha_g \alpha_l \bar{c}_{j,g}^g \bar{v}_g^g \right) - \left(\varepsilon_f \alpha_g \alpha_l \bar{c}_{j,1}^l \bar{v}_g^g + \varepsilon_f \alpha_l \alpha_g \bar{c}_{j,g}^g \bar{v}_1^1 \right) \\ &= \bar{c}_j \bar{v} + \varepsilon_f \alpha_g \alpha_l \left(\bar{c}_{j,1}^l - \bar{c}_{j,g}^g \right) \left(\bar{v}_1^1 - \bar{v}_g^g \right) \\ &= \bar{c}_j \bar{v} + \varepsilon_f \alpha_g \alpha_l \left(\bar{c}_{j,1}^l - \bar{c}_{j,g}^g \right) v_r, \end{aligned} \tag{A4}$$

where $v_r = \bar{v}_1^1 - \bar{v}_g^g$. Finally, the compressive advection term is written as

$$\nabla \cdot \left(\varepsilon_f \alpha_l \bar{c}_{j,1}^l \bar{v}_l^l + \varepsilon_f \alpha_g \bar{c}_{j,g}^g \bar{v}_g^g \right) = \nabla \cdot (\bar{c}_j \bar{v}) + \nabla \cdot \left(\varepsilon_f \alpha_g \alpha_l \left(\bar{c}_{j,1}^l - \bar{c}_{j,g}^g \right) v_r \right). \tag{A5}$$

2. Source terms in the saturation equation

When the density difference between the gas, liquid, and solid phases is large enough, using the explicit source term can easily cause numerical instability. To emphasize the role of the continuous equation when solving the saturation equation with source terms, $\alpha_l \nabla \cdot \bar{v} - \alpha_l \nabla \cdot \bar{v}$ is added to the right side of the saturation equation (34) as

$$\frac{\partial \varepsilon_f \alpha_l}{\partial t} + \nabla \cdot (\alpha_l \bar{v}) + \nabla \cdot (\varepsilon_f \alpha_l \alpha_g v_r) = \frac{\dot{m}_l}{\rho_l} + \alpha_l \nabla \cdot \bar{v} - \alpha_l \nabla \cdot \bar{v}. \tag{A6}$$

Then the second $\alpha_l \nabla \cdot \bar{v}$ is expanded using the continuous equation as

$$\frac{\partial \varepsilon_f \alpha_l}{\partial t} + \nabla \cdot (\alpha_l \bar{v}) + \nabla \cdot (\varepsilon_f \alpha_l \alpha_g v_r) = \frac{\dot{m}_l}{\rho_l} + \alpha_l \nabla \cdot \bar{v} - \alpha_l \left[\dot{m}_{\text{HCl}} \left(\frac{\gamma_s}{\rho_s} + \frac{\gamma_g}{\rho_g} + \frac{\gamma_l}{\rho_l} \right) \right]. \tag{A7}$$

Organize the right side of the equation, and merge the items containing α_l to obtain

$$\frac{\partial \varepsilon_f \alpha_l}{\partial t} + \boldsymbol{\nabla} \cdot (\alpha_l \bar{\boldsymbol{v}}) + \boldsymbol{\nabla} \cdot (\varepsilon_f \alpha_l \alpha_g \boldsymbol{v}_r) = \frac{\dot{m}_l}{\rho_l} + \alpha_l \left[\boldsymbol{\nabla} \cdot \bar{\boldsymbol{v}} - \dot{m}_{\text{HCl}} \left(\frac{\gamma_s}{\rho_s} + \frac{\gamma_g}{\rho_g} + \frac{\gamma_l}{\rho_l} \right) \right]. \qquad \text{(A8)}$$

The source term $\frac{\dot{m}_l}{\rho_l}$ is treated as an explicit term, and $\alpha_l [\boldsymbol{\nabla} \cdot \bar{\boldsymbol{v}} - \dot{m}_{\text{HCl}}(\frac{\gamma_s}{\rho_s} + \frac{\gamma_g}{\rho_g} + \frac{\gamma_l}{\rho_l})]$ is treated as an implicit term.

[1] H. Deng, J. Poonoosamy, and S. Molins, A reactive transport modeling perspective on the dynamics of interface-coupled dissolution-precipitation, Appl. Geochem. **137**, 105207 (2022).

[2] Y. Hao, M. M. Smith, and S. A. Carroll, Multiscale modeling of CO_2-induced carbonate dissolution: From core to meter scale, Int. J. Greenh. Gas Control. **88**, 272 (2019).

[3] X. Fu, L. Cueto-Felgueroso, D. Bolster, and R. Juanes, Rock dissolution patterns and geochemical shutdown of CO_2–brine–carbonate reactions during convective mixing in porous media, J. Fluid Mech. **764**, 296 (2015).

[4] H. Nie, C. Sun, G. Liu, W. Du, and Z. He, Dissolution pore types of the Wufeng Formation and the Longmaxi Formation in the Sichuan Basin, south China: Implications for shale gas enrichment, Mar. Pet. Geol. **101**, 243 (2019).

[5] S. Molins, D. Trebotich, L. Yang, J. B. Ajo-Franklin, T. J. Ligocki, C. Shen, and C. I. Steefel, Pore-scale controls on calcite dissolution rates from flow-through laboratory and numerical experiments, Environ. Sci. Technol. **48**, 7453 (2014).

[6] C. Soulaine, S. Roman, A. Kovscek, and H. A. Tchelepi, Mineral dissolution and wormholing from a pore-scale perspective, J. Fluid Mech. **827**, 457 (2017).

[7] T. Lei and K. H. Luo, Pore-scale simulation of miscible viscous fingering with dissolution reaction in porous media, Phys. Fluids **33**, 034134 (2021).

[8] S. Molins *et al.*, Simulation of mineral dissolution at the pore scale with evolving fluid-solid interfaces: Review of approaches and benchmark problem set, Comput. Geosci. **25**, 1285 (2021).

[9] X. Yang, H. Sun, Y. Yang, Y. Liu, and X. Li, Recent progress in multi-scale modeling and simulation of flow and solute transport in porous media, WIREs Water **8**, e1561 (2021).

[10] L. C. Ruspini *et al.*, Multiscale digital rock analysis for complex rocks, Transp. Porous Media **139**, 301 (2021).

[11] M. Liu and P. Mostaghimi, High-resolution pore-scale simulation of dissolution in porous media, Chem. Eng. Sci. **161**, 360 (2017).

[12] F. Gray, B. Anabaraonye, S. Shah, E. Boek, and J. Crawshaw, Chemical mechanisms of dissolution of calcite by HCl in porous media: Simulations and experiment, Adv. Water Resour. **121**, 369 (2018).

[13] B. Guo, L. Ma, and H. A. Tchelepi, Image-based micro-continuum model for gas flow in organic-rich shale rock, Adv. Water Resour. **122**, 70 (2018).

[14] K. Miller, T. Vanorio, S. Yang, and X. Xiao, A scale-consistent method for imaging porosity and micrite in dual-porosity carbonate rocks, Geophysics **84**, MR115 (2019).

[15] F. J. Carrillo, I. C. Bourg, and C. Soulaine, Multiphase flow modeling in multiscale porous media: An open-source micro-continuum approach, J. Comput. Phys.: X **8**, 100073 (2020).

[16] C. Soulaine, P. Creux, and H. A. Tchelepi, Micro-continuum framework for pore-scale multiphase fluid transport in shale formations, Transp. Porous Media **127**, 85 (2019).

[17] C. Soulaine, S. Roman, A. Kovscek, and H. A. Tchelepi, Pore-scale modelling of multiphase reactive flow: Application to mineral dissolution with production CO_2, J. Fluid Mech. **855**, 616 (2018).

[18] C. Noiriel and C. Soulaine, Pore-scale imaging and modelling of reactive flow in evolving porous media: Tracking the dynamics of the fluid–rock interface, Transp. Porous Media **140**, 181 (2021).

[19] Z. Liu, J. Yang, Q. Xu, and L. Shi, Improved micro-continuum approach for capillary-dominated multiphase flow with reduced spurious velocity, Phys. Fluids **34**, 122108 (2022).

[20] Q. Xu, X. Dai, J. Yang, Z. Liu, and L. Shi, Image-based modelling of coke combustion in a multiscale porous medium using a micro-continuum framework, J. Fluid Mech. **932**, A51 (2022).

[21] L. Chen, Q. Kang, B. A. Robinson, Y. L. He, and W. Q. Tao, Pore-scale modeling of multiphase reactive transport with phase transitions and dissolution-precipitation processes in closed systems, Phys. Rev. E **87**, 043306 (2013).

[22] Q. Xu, L. Guan, W. Zhang, L. Shi, H. Shao, G. Wang, and W. Long, Multiscale digital rock imaging and modeling for measuring the heterogeneous carbonate and conglomerate permeability at the laboratory plug scale, Energy Fuels **36**, 11025 (2022).

[23] M. Miarelli and A. Della Torre, Workflow development to scale up petrophysical properties from digital rock physics scale to laboratory scale, Transp. Porous Media **140**, 459 (2021).

[24] T. D. Scheibe, W. A. Perkins, M. C. Richmond, M. I. McKinley, P. D. J. Romero-Gomez, M. Oostrom, T. W. Wietsma, J. A. Serkowski, and J. M. Zachara, Pore-scale and multiscale numerical simulation of flow and transport in a laboratory-scale column, Water Resour. Res. **51**, 1023 (2015).

[25] S. Molins, D. Trebotich, B. Arora, C. I. Steefel, and H. Deng, Multi-scale model of reactive transport in fractured media: Diffusion limitations on rates, Transp. Porous Media **128**, 701 (2019).

[26] G. S. Beavers and D. D. Joseph, Boundary conditions at a naturally permeable wall, J. Fluid Mech. **30**, 197 (2006).

[27] T. D. Scheibe, K. Schuchardt, K. Agarwal, J. Chase, X. Yang, B. J. Palmer, A. M. Tartakovsky, T. Elsethagen, and G. Redden, Hybrid multiscale simulation of a mixing-controlled reaction, Adv. Water Resour. **83**, 228 (2015).

[28] F. Yang, A. G. Stack, and V. Starchenko, Micro-continuum approach for mineral precipitation, Sci. Rep. **11**, 3495 (2021).

[29] P. Horgue, M. Prat, and M. Quintard, A penalization technique applied to the "Volume-Of-Fluid" method: Wettability condition on immersed boundaries, Comput. Fluids **100**, 255 (2014).

[30] Y. Haroun, D. Legendre, and L. Raynal, Volume of fluid method for interfacial reactive mass transfer: Application to stable liquid film, Chem. Eng. Sci. **65**, 2896 (2010).

[31] L. Yang, M. J. Nieves-Remacha, and K. F. Jensen, Simulations and analysis of multiphase transport and reaction in segmented flow microreactors, Chem. Eng. Sci. **169**, 106 (2017).

[32] J. Maes and C. Soulaine, A new compressive scheme to simulate species transfer across fluid interfaces using the volume-of-fluid method, Chem. Eng. Sci. **190**, 405 (2018).

[33] F. J. Carrillo, *Modeling Multiphase Flow Through and Around Multiscale Deformable Porous Materials* (Princeton University Press, Princeton, NJ, 2021).

[34] R. H. Brooks, *Hydraulic Properties of Porous Media* (Colorado State University Press, Fort Collins, CO, 1965).

[35] M. T. Van Genuchten, A closed-form equation for predicting the hydraulic conductivity of unsaturated soils, Soil Sci. Soc. Am. J. **44**, 892 (1980).

[36] J. Maes and C. Soulaine, A unified single-field Volume-of-Fluid-based formulation for multi-component interfacial transfer with local volume changes, J. Comput. Phys. **402**, 109024 (2020).

[37] Q. Xu, W. Long, H. Jiang, B. Ma, C. Zan, D. Ma, and L. Shi, Quantification of the microstructure, effective hydraulic radius and effective transport properties changed by the coke deposition during the crude oil in-situ combustion, Chem. Eng. J. **331**, 856 (2018).

[38] J. Maes and H. P. Menke, GeoChemFoam: Direct modelling of multiphase reactive transport in real pore geometries with equilibrium reactions, Transp. Porous Media **139**, 271 (2021).

[39] H. Jasak, Ph.D. thesis, Imperial College London, 1996.

[40] H. G. Weller, G. Tabor, H. Jasak, and C. Fureby, A tensorial approach to computational continuum mechanics using object-oriented techniques, Comput. Phys. **12**, 620 (1998).

[41] H. Jasak, A. Jemcov, and Z. Tukovic, in *International Workshop on Coupled Methods in Numerical Dynamics* (IUC Dubrovnik, Croatia, 2007), Vol. 1000, pp. 1–20.

[42] B. Van Leer, Towards the ultimate conservative difference scheme, J. Comput. Phys. **135**, 229 (1997).

[43] GeoChemFoam User Guide, https://github.com/GeoChemFoam/GeoChemFoam/blob/main/ GeoChemFoam-User-Guide.pdf.

[44] H. G. Weller, A new approach to VOF-based interface capturing methods for incompressible and compressible flow, Technical Report No. TR/HGW/04 (OpenCFD, Salfords, UK, 2008).

[45] R. I. Issa, Solution of the implicitly discretised fluid flow equations by operator-splitting, J. Comput. Phys. **62**, 40 (1986).

[46] See Supplemental Material at http://link.aps.org/supplemental/10.1103/PhysRevFluids.9.043801 for boundary condtions, simulation parameters, and mesh independence test.

[47] M. Graveleau, C. Soulaine, and H. A. Tchelepi, Pore-scale simulation of interphase multicomponent mass transfer for subsurface flow, Transp. Porous Media **120**, 287 (2017).

[48] J. Yang, X. Dai, Q. Xu, Z. Liu, L. Shi, and W. Long, Lattice Boltzmann modeling of interfacial mass transfer in a multiphase system, Phys. Rev. E **104**, 015307 (2021).

[49] P. Horgue, C. Soulaine, J. Franc, R. Guibert, and G. Debenest, An open-source toolbox for multiphase flow in porous media, Comput. Phys. Commun. **187**, 217 (2015).

[50] H. Deng, S. Molins, C. Steefel, D. DePaolo, M. Voltolini, L. Yang, and J. Ajo-Franklin, A 2.5D reactive transport model for fracture alteration simulation, Environ. Sci. Technol. **50**, 7564 (2016).

[51] C. Noiriel, L. Luquot, B. Madé, L. Raimbault, P. Gouze, and J. Van Der Lee, Changes in reactive surface area during limestone dissolution: An experimental and modelling study, Chem. Geol. **265**, 160 (2009).